ECCENTRIC COMPRESSIVE BEHAVIOUR OF ELLIPTICAL FRP TUBE-CONFINED REINFORCED-CONCRETE COLUMNS

K.C. Liu, T. Yu* and J.G. Teng*

ABSTRACT

Elliptical FRP-tube confined reinforced concrete columns (EFCRCCs) are an emerging form of columns particularly suitable for use where the required resistances differ substantially in the two orthogonal lateral directions. This paper first presents a systematic experimental study on the eccentric compressive behaviour of EFCRCCs, with the main test variables being the initial load eccentricity, the sectional aspect ratio, the bending direction and the fibre orientations of the FRP tube. The test results showed that EFCRCCs possessed excellent structural performance, including ample ductility under eccentric compression; the effects of the key test variables on the eccentric compressive behaviour of EFCRCCs were also clarified. A theoretical model developed for EFCRCCs, with the slenderness effect taken into consideration, is then presented. The theoretical model is shown to provide reasonably accurate and conservative predictions of the load-carrying capacity of EFCRCCs. Using this theoretical model, the effects of stress-strain behaviour of the confined concrete in EFCRCCs on their eccentric compressive behaviour are examined, which provides valuable information for the establishment of an accurate stress-strain model for the concrete in eccentrically loaded EFCRCCs.

Keywords

Elliptical Column; FRP; Concrete; Confinement; Eccentric Compression; Strain Gradient Effect.

1 INTRODUCTION

Elliptical fibre-reinforced polymer (FRP) tube-confined reinforced concrete columns (EFCRCCs) are an emerging form of columns recently developed at The Hong Kong Polytechnic University (Liu et al., 2023; Liu, 2023). An EFCRCC consists of an elliptical FRP outer tube and a concrete infill reinforced with longitudinal steel bars, and can be considered as a variation of circular concrete-filled FRP tubes (CFFTs) which have received increasing attention since the late 1990s (e.g., Saafi et al.,1999; Ozbakkaloglu and Saatcioglu, 2006; Yu and Teng, 2011). Compared to circular CFFTs, EFCRCCs are particularly suitable for use where the required resistances differ substantially in the two orthogonal lateral directions. In EFCRCCs, the FRP tube serves as an anti-corrosion protective layer, a stay-in-place formwork, and a confining device for the internal concrete; such an FRP tube typically has fibres close to the hoop direction and can be easily fabricated via a filament-winding process.

The effectiveness of FRP confinement in an elliptical column has been demonstrated by several existing studies (Teng and Lam, 2002; Teng et al., 2016; Chen et al., 2021) on wet lay-up FRP-wrapped concrete columns, and more recently, by Liu et al. (2023) through a series of axial compression tests on filament-wound FRP tube-confined concrete columns. The axial stress-strain behaviour of FRP-confined concrete in elliptical columns has been investigated in these studies, yielding several design-oriented stress-strain models (Teng et al., 2016; Cao et al., 2016; Chen et al., 2021; Liu et al., 2023; Liu, 2023), among which a model proposed by the authors' group has been adopted by the relevant Chinese national standard GB50608 (GB 2020).

Furthermore, Chen et al. (2023) tested a few FRP-wrapped elliptical column specimens under cyclic axial compression, and showed that cyclic loading had marginal effects on the FRP confinement. Zhang et al. (2023) tested a number of EFCRCCs under combined constant axial compression and cyclic lateral loading, and demonstrated the excellent ductility of the columns. In addition, a few recent studies (Zhang et al. 2020; Chen et al. 2022) have been conducted on elliptical FRP-concrete-steel double-skin tubular columns, which may be considered a variation of EFCRCCs.

No existing studies have been conducted on the eccentric compressive behaviour of EFCRCCs. In reality, however, almost all columns are considered to be subjected to a certain load eccentricity due to either design requirements or the presence of construction imperfections (Parvin and Wang, 2001). The bending action due to the load eccentricity can significantly affect the structural behaviour of columns and may be significantly amplified by the column slenderness effect (Claeson and Gylltoft, 1998; Mirmiran et al., 2001; Xing et al., 2020). In most design codes/guidelines (e.g., BSI, 2004; ACI, 2019; GB, 2020), a minimum load eccentricity is specified even for a column intended to resist a nominally concentric load, and an additional load eccentricity or a moment magnification factor is usually adopted to account for the slenderness effect. Therefore, a robust design procedure for EFCRCCs must consider the effects of load eccentricity and column slenderness.

Many studies have been conducted on the eccentric compressive behaviour of FRP-confined concrete columns with a circular, square or rectangular shape (e.g., Hadi, 2006; Bisby and Ranger, 2010; Csuka and Kollár, 2011; Shaikh and Alishahi, 2019; Lin and Teng, 2017; Lin et al., 2020). These studies have shown that the presence of a load eccentricity may affect: (1) the efficiency of FRP confinement; and (2) the axial stress-strain behaviour of confined concrete. Several stress-strain models that can consider the effects of load eccentricity have been proposed in some of these studies for FRP-confined concrete in circular columns and some of them can provide reasonably accurate predictions (e.g., Lin and Teng, 2019). As expected, the effects of load eccentricity are related to the sectional shape of the column (Jiang and Wu, 2020; Tijani et al., 2022). Therefore, the conclusions from, and the models developed by, the existing studies on columns of circular and rectangular sections under eccentric compression are not directly applicable to elliptical columns under eccentric compression. To the best of the authors' knowledge, no studies have investigated the effects of load eccentricity on the structural behaviour of EFCRCCs. Against this background, this paper presents a combined experimental and theoretical study with a focus on clarifying the effects of load eccentricity on EFCRCCs.

2 EXPERIMENTAL PROGRAMME

2.1 Specimen Details

A total of 18 EFCRCC specimens were prepared and tested. Details of all the specimens are summarised in Table 1. The test variables included: (1) the aspect ratio of the cross-section a/b (a is half of the length of the major axis; b is half of the length of the minor axis); (2) the orientations of fibres in the FRP tube; (3) the bending direction; and (4) the initial load eccentricity (e_i). All the specimens were 900 mm in height and had the same nominal major-axis length ($2a$) of 300 mm, while they had a nominal minor-axis length ($2b$) of either 200 mm or 150 mm, leading to an aspect ratio of 1.5 or 2.0.

The specimens were each internally reinforced with eight longitudinal steel rebars. No internal lateral steel reinforcement (e.g., steel stirrups) was used so that the confinement to the concrete was only from the FRP tube (Figure 1). The diameters of steel rebars in the specimens with aspect ratios of 1.5 and 2.0 were 18 mm and 16 mm, respectively, leading to a similar reinforcement ratio (i.e., 4.32% and 4.55%, respectively, for the two section configurations) for ease of comparison. The specimens were classified into three groups (i.e., Group A, B, and C) (Table 1), with the differences between different groups being the aspect ratio of the section and/or the fibre orientations of FRP tube: Group A specimens had an aspect ratio of 1.5 and fibre orientations of ±80° to the longitudinal axis; Group B specimens had an aspect ratio of 2.0 and fibre orientations of ±80°; Group C specimens had an aspect ratio of 1.5 and fibre orientations of ±60°. The six specimens in each group were nominally identical, and their tests covered three initial load eccentricities (i.e., 25 mm, 50 mm and 120 mm) for bending in the major axis direction (hereafter referred to as major-axis bending), two initial load eccentricities (i.e., 25 mm and 50 mm) for bending in the minor axis direction (hereafter referred to as minor-axis bending), and a concentric compression test for comparison.

Each specimen is given a name, which includes a letter "E" plus a two-digit number denoting the aspect ratio of the cross-section, a letter "F" plus a two-digit number denoting the fibre orientations, a letter "S" (denoting the strong direction of bending, also referred to as major-axis bending) or "W" (denoting the weak direction of bending, also referred to as major-axis bending), and a final two- or a three-digit number denoting the initial load eccentricity. For instance, E15F60-W25 denotes a specimen that had a sectional aspect ratio of 1.5, an FRP tube with fibre orientations of ±60˚ and was loaded eccentrically with an initial load eccentricity of 25 mm on the minor axis.

2.2 Material Properties

2.2.1 Concrete

All the specimens were cast using the same batch of commercial concrete, the mix proportions of which are given in Table 2. Testing of the specimens began on the 28th day after casting and lasted for another 28 days. The specimens of Group A were tested within the first 14 days; the remaining specimens were tested within the second 14 days. The concrete properties were obtained on both the 28th and the 42nd days after casting to capture variations induced by time. On each of these two concrete property test days, three standard concrete cylinders were tested to determine the compressive strength (f'_{co}) and the corresponding axial strain at peak stress (ε_{co}) in accordance with ASTM (2016a), and the compressive elastic modulus (E_c) and the Poisson's ratio (ν) in accordance with ASTM (2014). The obtained concrete properties are detailed in Table 3. It can be seen that the concrete compressive strength increased slightly with time, while the other properties did not exhibit much variation.

2.2.2 FRP

The FRP tubes were made of glass fibres (i.e., GFRP tubes) via a filament-winding process. The GFRP tubes with fibre orientations of ±80° were produced using the hoop winding method, while those with fibre orientations of ±60° were made using the helical winding method (Rejab et al., 2008). All the GFRP tubes had six layers of fibres (see Table 1). The thickness of each GFRP tube, which was averaged from measurements at several locations using a Vernier calliper, are listed in Table 1. It was observed that the thickness of FRP tubes with fibre orientations of ±60° was generally greater than that of the tubes with fibre orientations of ±80°, due mainly to the difference in the amount of matrix resin as a result of the different winding methods. The nominal layer thicknesses are 0.50 mm for the 60° fibre layer and 0.35 mm for the 80° fibre layer. Curved coupon tests [in accordance with Teng et al. (2023)] were conducted to determine the elastic modulus of the GFRP tubes in the hoop direction, while compression tests on FRP rings [in accordance with GB/T 5350 (GB/T 2005)] were conducted to determine the properties of the GFRP tubes in the axial direction. The test results are given in Table 4, where $E_{FRP,h}$ represents the hoop elastic modulus; $E_{FRP,a}$ represents the axial elastic modulus; $t_{FRP,h}$ and $t_{FRP,a}$ are the average thickness of test specimens in the two types of tests, respectively. Readers may refer to Liu et al. (2023) for more details of these FRP tube material property tests.

2.2.3 Steel

The properties of steel rebars were determined by the tensile tests in accordance with ASTM (2016b). The yield strain (ε_y), yield stress (f_y), tensile strength (f_{su}), elastic modulus (E_s), and their average values are detailed in Table 5.

2.3 Preparation of Column Specimens

The preparation of column specimens involved the following steps: (1) welding the longitudinal steel rebars to a bottom steel plate of 40 mm in thickness through predrilled holes (Figure 2a); (2) placing the FRP tube at a pre-defined position and toping it with a top steel plate of 20 mm in thickness having predrilled holes and a rectangular opening (Figure 2b); (3) welding the steel rebars to the top plate through the predrilled holes (Figure 2c); (4) fixing the FRP tube with the short positioning steel bars welded on the two steel plates, and sealing the joints between the FRP tube and the two steel plates (Figure 2d); (5) casting concrete through the rectangular opening on the top plate (Figure 2e); (6) strengthening each of the column ends with a three-layer carbon FRP (CFRP) strip of 35 mm in strip width. It should be noted that the above preparation process aimed at ensuring a direct transfer of tensile forces between the top or the bottom plate and the steel rebars during loading. This is essential in such column tests as the steel rebars serve as the main longitudinal reinforcement. The longitudinal connection between the FRP tube and the steel plates to transfer stresses was not necessary as their main function was to confine the concrete, but some tensile forces were still transferred to the FRP tube from the concrete core through the interfacial friction between the two. Nevertheless, the tensile stress transfer to the FRP tube is not important phenomenon in these column tests due to the small cross-sectional area and axial stiffness of the FRP tube.

2.4 Test Setup and Instrumentation

Linear Variable Differential Transformers (LVDTs) and strain gauges were used to monitor the deformation of each column specimen. The layouts of LVDTs and strain gauges are illustrated in Figures 3 and 4, respectively. For column specimens subjected to concentric loading, four LVDTs were used for measuring the axial deformation of the 240 mm mid-height region (LVDTs 1-4) and another two were used for measuring the full-height axial shortening (LVDTs 5 & 6). For column specimens subjected to eccentric loading, two more LVDTs (LVDTs 7 & 8) were used to measure the rotations at specimen ends, and another two LVDTs (LVDTs 9 & 10) were used to monitor the lateral displacements at the mid-height of the specimen (see Figure 3). Eight axial strain gauges and 16 hoop strain gauges with a gauge length of 20 mm were installed over the circumference at or close to the mid-height of the specimen (Level 1). Four axial strain gauges with a gauge length of 20 mm were installed at the four vertices of two other heights (i.e., 300 mm above and below the mid-height of the specimen, respectively, referred to as Level 2 hereafter) (see Figure 4a). In addition, two axial strain gauges with a gauge length of 5 mm were installed on each steel rebar at the mid-height section (i.e., Level 1) (see Figure 4b). Before testing, an additional 20 mm-thick steel plate was bolted to the top steel plate with four threaded fasteners at the corners to replicate the boundary condition of the column footing (see Figure 3a).

The eccentrically loaded column specimens were compressed through two hinges at the two ends, respectively (Figure 3b). Same as those under concentric compression, an additional 20-mm thick steel plate was bolted to the top steel plate with four threaded fasteners at the corners to replicate the boundary condition of the column footings (see Figure 3b). When testing the column specimens under concentric compression, the hinges were removed and replaced by high-strength plaster for levelling. All the column specimens were tested using a compression testing machine with a nominal load capacity of 8000 kN. The column specimens were monotonically loaded with displacement control at a constant rate of 0.36 mm/min.

3 TEST OBSERVATIONS, RESULTS AND DISCUSSIONS

3.1 Test Observations and Failure Modes

3.1.1 Concentrically loaded specimens

Figure 5 shows the specimens under concentric loading (i.e., E15F80-S00; E20F80-S00; and E15F60-S00) after testing. These specimens all failed by the rupture of FRP tube accompanied by an explosive noise and a severe load drop. As the FRP tube ruptured, the inner concrete collapsed, and the steel rebars buckled due to the sudden loss of lateral support from concrete. The explosive noise of Specimen E20F80-S00 and E15F60-S00 was found to be milder compared to that of E15F80-S00 due to the relatively high level of confinement of the latter. Besides, the FRP rupture in Specimen E20F80-S00 was concentrated at one of the major-axis vertices. In contrast, the FRP rupture in Specimen E20F80-S00 initiated near the top end rather than in the middle region. This discrepancy may be attributed to local defects in the FRP tube, which could have resulted in a lower rupture strain at that specific location.

3.1.2 Eccentrically loaded specimens

The failure modes of the eccentrically loaded specimens are shown in Figure 6. It can be seen that the fibre orientations of the GFRP tube significantly affected the failure mode of the specimen. The specimens with fibre orientations of ±80° (Group A & Group B) eventually failed by the rupture of GFRP tube at or near the mid-height section on the compression side. It was observed during testing that tensile cracks parallel to the fibre orientations initiated on the tension side of the FRP tube during the early loading stage; the cracks then gradually extended towards the compression side as the loading continued. However, these tensile cracks did not appear to affect the load carried by the specimen, as no load fluctuation was observed until failure. In addition, for the specimens under minor-axis bending, some wrinkles on the compression side of the FRP tube were observed before failure due to large bending deformation. As expected, the lateral deflection of the specimen as well as the density and size of the tensile cracks on the tension side of the FRP tube, when the FRP tube reached hoop tensile rupture on the compression side, increase with the initial load eccentricity e_i (Figures 6a-c).

For the specimens with fibre orientations of ±60° (Group C), no apparent cracks on the tension side of the FRP tube were observed during testing, indicating that the damage of resin in the FRP tube was well controlled by the fibres. With the increase of loading, the colour of the FRP tube on the compression side gradually turned white, suggesting that the damage of FRP was accumulating. The column specimens under major-axis bending eventually failed by the rupture of GFRP tube on the compression side due to the expansion of concrete, which was followed by the rapid development of cracks towards the tension side along the direction of fibres (see Figures 6a & 6b). By contrast, the specimens under minor-axis bending eventually failed by the abrupt rupture of fibres on the tension side due to longitudinal tension (see Figures 6d & 6e), which was associated with a sudden load drop. It should be noted that specimen E15F60-S120 failed prematurely during the early testing stage due to the fracture of welds between the steel rebars and the upper steel plate (see Figure 6c); this specimen is thus not further discussed hereafter.

3.2 Test Results and Discussions

3.2.1 Key results

Table 6 provides the key column test results of the experimental programme. In Table 6, F_{max} is the peak axial load carried by the specimen; M_{Fmax} and Δ_{Fmax} are the total bending moment and the lateral displacement corresponding to F_{max} at the mid-height section of the specimen, respectively; F_u and Δ_u are the axial load carried by the specimen and the lateral displacement at the mid-height section at the ultimate state, respectively. The ultimate state is defined as the state when the fibres in the FRP tube ruptured on the compression side or the tension side associated with a sudden load drop; ε_{cu} represents the axial strain of the extreme compression fibre (ECF) (i.e., the point farthest from the neutral axis on the compression side) at the mid-height of an eccentrically loaded specimen or the average axial strain at the mid-height of a concentrically loaded specimen at the ultimate state [For concentrically loaded specimens, ε_{cu} refers to the average axial strain measured by the LVDTs (i.e., LVDTs 1-4, see Figure 3) at the mid-height region at the ultimate state; for eccentrically loaded specimens, ε_{cu} refers to the ultimate axial strain of ECF measured by LVDT 1 and LVDT 4 for specimens under major- and minor-axis bending, respectively]; $\varepsilon_{hu,max}$ is the maximum hoop strain measured by the hoop strain gauges at the mid-height section of a specimen at the ultimate state; M_i and M_Δ are the primary moment and the second-order moment, which are equal to the axial load (F) multiplied by the initial load eccentricity (e_i) and the lateral displacement at the mid-height section (Δ), respectively, as expressed in the equation below for the total bending moment (M):

$$M = M_i + M_\Delta = F \times \left(e_i + \Delta\right) \tag{1}$$

It should also be noted that the $\varepsilon_{hu,max}$ values in Table 6 do not always represent the actual maximum hoop strain of the mid-height section as some strain gauges had already malfunctioned before the ultimate state. The non-functional hoop strain gauges at the ultimate state of each specimen are also listed in Table 6.

3.2.2 Effects of load eccentricity

Figures 7 and 8 show the load-displacement curves of specimens under major-axis bending and minor-axis bending, respectively. The curves of the nominally identical specimens in each group (i.e., Group A, B or C) are shown in the same subfigure to illustrate the effect of initial load eccentricity (e_i), and these curves all terminate at the ultimate state (i.e., FRP rupture). In these figures, the axial displacement represents the full-height axial shortening of the specimen taken as the average reading of LVDTs 5 and 6 (see Figure 3); the lateral displacement represents that at the mid-height of the specimen as averaged from the readings of LVDTs 9 and 10 (see Figure 3).

<u>Major-axis bending versus minor-axis bending</u>

Figure 7 shows that the curves of specimens under major-axis bending generally consist of two branches: (1) an initial approximately linear branch; and (2) a second branch which is generally ascending but with a decreasing slope. It is evident from the ascending second branch that the FRP confinement is still effective for EFCRCCs under eccentric loading, while its decreasing slope is at least partially due to the increasing lateral deflection and the resultant second-order bending moment. As expected, the load capacity and the stiffness (indicated by the slope of the axial load-displacement curve) of the specimens generally decrease with e_i. The deformation capacity of the specimens, as indicated by the axial and lateral displacements at the ultimate state, however, generally increases with e_i except for Specimen E20F80-S50, which failed at an unusually low hoop rupture strain (see Table 6). The above observation is generally consistent with that reported in previous studies on FRP-confined concrete circular columns (Hadi, 2007a; Bisby and Ranger, 2010; Csuka and Kollár, 2011; Song et al., 2013; Lin and Teng, 2019; Xing et al., 2020).

By contrast, Figure 8 shows that the curves of the specimens under minor-axis bending generally feature a descending branch before the ultimate state. The slope of the initial branch of the curves and the load capacity of these specimens still decrease with e_i, while the slope of the descending branch of the curves does not seem to be evidently related to e_i. The latter observation is due to the relatively large lateral deflection during the later stage of loading, which makes the second-order bending moment dominant during this stage (Xing et al., 2020; Khorramian and Sadeghian, 2021). It is also evident that the load-carrying capacity of a specimen under minor-axis bending is much lower than that of its counterpart under major-axis bending with the same load eccentricity (see Table 6 and Figures 7 and 8).

The evident differences in behaviour between the specimens under minor- and those under major-axis loadings are mainly due to the smaller bending stiffness of the former, which makes the second-order effect more pronounced in the former. The second-order effect on a column is commonly considered in design using the so-called slenderness ratio, which is calculated as kl/r, where k is the effective length factor (e.g., equal to 0.5 for columns with fixed ends and 1.0 for columns with pinned ends), l is the column length, and r is the radius of gyration whose value depends on the direction of buckling deformation that is being considered (ACI, 2019; GB 50608, 2020). For elliptical columns, the r value can be calculated as $a/2$ for bending in the major axis direction and as $b/2$ for bending in the minor axis direction (Ram, 2012). Details of the calculation are given in the Appendix. The slenderness ratios (kl/r) of all the test specimens are given in Table 1, where the differences in the slenderness ratio value between the specimens under minor- and major-axis bending are evident.

The differences in behaviour between the two types of specimens (i.e., under minor- and major-axis bending, respectively) are also believed to be partially due to the non-uniform confinement to the concrete in EFCRCCs. For the specimens under minor-axis bending, the concrete near one of the minor-axis vertexes is the most severely compressed but also the most weakly confined by the FRP tube in EFCRCCs due to the large radius of curvature of the FRP tube in that region (Teng et al., 2016). By contrast, the most-compressed concrete in the specimens under major-axis bending is close to one of the major-axis vertices, which is also the most effectively confined region in the section (Teng et al., 2016).

<u>Ultimate axial strain</u>

The ultimate axial strain (ε_{cu}) of each specimen is given in Table 6. It is evident from the results in Table 6 that, for the specimens failing by FRP rupture on the compression side, the so-obtained axial strain at the point of FRP rupture generally increases with e_i, except for Specimen E20F80-S50, which failed at an unusually small hoop strain as explained earlier, and Specimen E15F80-W50. This observation is consistent with those from previous studies on FRP-confined concrete columns of other shapes (i.e., circular and rectangular columns) (Hadi, 2006; Hadi, 2007a, 2007b; Bisby and Ranger, 2010; Csuka and Kollár, 2011; Hadi and Widiarsa, 2012; Lin et al., 2020; Jiang and Wu, 2020; Xing et al., 2020; Tijani et al., 2022) and is believed to be due to the existence of a strain gradient which leads to reduced lateral expansion of concrete on the compression side for the same axial strain. By contrast, for the two specimens failing by FRP rupture on the tension side (i.e., Specimens E15F60-W25 and E15F60-W50), the ultimate axial strain does not seem to be significantly affected by e_i. This is not a surprise as FRP rupture in these columns was not induced by the lateral expansion of concrete.

3.2.3 Effects of aspect ratio and fibre orientations

Figure 9 illustrates the effects of aspect ratio (a/b) and fibre orientations of the FRP tube on the load-displacement behaviour of EFCRCCs. The curves of the specimens tested under the same e_i are shown in the same subfigure for comparison.

It is not a surprise to see that the curves of specimens of Group B with an aspect ratio of 2.0 are evidently lower than their counterparts in Group A with an aspect ratio of 1.5 due to the smaller cross-section area of the former. In addition, the second-branch slope of the curves of Group B specimens is generally smaller than that of the corresponding specimens in Group A, suggesting that the confinement effect of the FRP tube is more pronounced in the latter. By contrast, the ultimate axial displacement of Group B specimens under eccentric compression is generally larger than their Group A counterparts. The axial displacement was averaged from LVDTs 5 and 6, representing the shortening of the column between the two loading points. The relatively large ultimate axial displacement of Group B specimens is believed to be at least partially due to their relatively small column bending stiffness.

The only difference between Group A and Group C specimens is the fibre orientations of the FRP tube. Figure 9 shows that the fibre orientations mainly affect the second branch of the load-displacement curves: both its slope and peak point (i.e., load capacity) increase with the fibre angles due to the enhanced confinement effect of the FRP tube. As the fibre angle increases, the longitudinal stiffness of FRP tube decreases while the confinement effect increases; Figure 9 shows that the confinement effect is more beneficial on the eccentric compressive behaviour of EFCRCCs.

It is also evident from Figure 9 that the effect of fibre orientations on the ultimate axial displacement of EFCRCCs depends on e_i. Under concentric loading (i.e., e_i = 0), the ultimate displacement of the specimen with fibre angles of ±60° is much smaller than that of the corresponding specimen with the fibre angles of ±80° (see Figure 9a). This observation is consistent with those made by Liu et al. (2023) and in other experimental studies on FRP-confined circular concrete columns (e.g., Vincent and Ozbakkaloglu, 2013; Hain et al., 2019). By contrast, when e_i is not zero (i.e., eccentric loading), the ultimate axial displacement of the specimens confined by an FRP tube with fibre orientations of ±60° is generally larger than that of their counterparts with fibre orientations of ±80° (e.g., Figure 9b).

To further examine the effects of aspect ratio and fibre orientations on the peak load of EFCRCCs under eccentric compression, the normalised peak load ($F_{max}/F_{max,c}$) was plotted against the nominalised initial load eccentricity (e_i/D) in Figure 10; here, the peak load F_{max} is normalised by the peak load $F_{max,c}$ of the corresponding concentrically loaded specimen while the initial load eccentricity e_i is normalised by the length of the axis (D) on which e_i is located. It is evident from Figure 10 that the peak load decreases with e_i for all three groups. Furthermore, the decrease appears to be most pronounced for Group A, in which the confinement provided by the FRP tube was the strongest. Similar observations have also been reported in previous studies on FRP-confined circular reinforced concrete (RC) columns [e.g., Bisby and Ranger (2010); Hadi (2007b)].

Figure 11 illustrates the effects of aspect ratio and fibre orientations on the ultimate compressive strain of EFCRCCs under eccentric compression. In Figure 11, the ultimate axial strain obtained by the LVDT installed at the ECF of the eccentrically loaded specimens is shown against the normalised load eccentricity (e_i/D). For ease of comparison, these axial strains are normalised by the average ultimate axial strain measured by the LVDTs at the mid-height of the corresponding concentrically loaded specimen. It is evident that the ultimate axial strain generally increases with the load eccentricity, and such increases appear to be more pronounced for specimens with a larger aspect ratio (Group B) or a smaller angle of fibres (Group C).

3.2.4 Axial strain distribution over the mid-height section

Figure 12 shows the typical axial strain distributions over the mid-height section, using Specimen E15F80-S25 (Group A) as an example. The axial strain distributions of other specimens are generally similar (see Figure A3 in the Appendix). In Figure 12, the solid and hollow symbols represent the readings of strain gauges installed on the FRP tube and the steel rebars, respectively; the AS value is the full-height axial shortening measured by LVDTs 5 & 6 (see Figure 3). It can be seen from Figure 12 that except for some scatter of strain gauge readings during the late stage of loading, the axial strain distribution along the direction of eccentricity is generally linear during the whole loading process, suggesting that the plane section assumption is valid. The scatter of strain gauge readings during the late loading stage is due to localised damage of the concrete and/or FRP tube as discussed earlier.

4 THEORETICAL ANALYSES

4.1 Sectional Analyses

For short FRP-confined RC columns subjected to eccentric compression, the load capacity can be evaluated by constructing the axial load–bending moment (N-M) interaction diagram using the traditional sectional analysis approach based on the plane section assumption (Rocca et al. 2009; Carrazedo and de Hanai, 2017). The key to the success of such sectional analysis is the use of an accurate uniaxial stress-strain curve for the confined concrete. In this study, a sectional analysis of EFCRCCs was conducted, making use of the model proposed by Liu et al. (2023) for the compressive behaviour of the confined concrete (hereafter referred to as Model I). It should be noted that two stress-strain models [i.e., Model I and the model adopted by GB50608 (GB 2020)] have been developed by the authors' group, among which Model I provides more accurate predictions in terms of the second slope and the whole stress-strain curve and is thus used here; the model in GB50608 (GB 2020) was formulated with the accurate prediction of the section strength as the top priority rather than the stress-strain path, and is thus more suitable for strength design based on the ultimate state. Furthermore, Model I has been found to provide reasonably accurate predictions of the test results of the concentrically loaded specimens (i.e., Specimen E15F80-S00; E20F80-S00; E15F60-S00) presented in this study. The results are given in the Appendix (see Figure A1) without further discussion as a comprehensive study on the performance of this model as well as other available models has been given in the previous study of the authors (Liu et al., 2023). In this sectional analysis, the unconfined strength was taken as 0.85 times the strength obtained from the standard cylinder (150 mm x 300 mm) tests to account for the size effect (e.g., Popovics 1998). The tensile strength of concrete is ignored. The steel rebars are treated as an elastic-perfect plastic material, and their stress-strain curve can be determined using the material properties listed in Table 5. The direct contribution of FRP tubes in the axial direction is ignored due to its small cross-section area and small axial stiffness.

Figure 13 shows the *N-M* interaction diagram predicted by the sectional analysis. The experimental axial load-bending moment loading paths of the test specimens were also plotted in the same figure for comparison, in which the bending moment represents the total moment of the mid-height section including that induced by the lateral displacement (i.e., second-order moment); the experimental loading paths are terminated at the ultimate state (i.e., FRP rupture). Furthermore, the predicted peak load of each test specimen, which is taken as the load at the interception point between the load path determined by the initial load eccentricity (represented by a straight grey line) and the predicted *N-M* interaction diagram, is given in Table 7.

It is evident from Figure 13 that: (1) the experimental loading path deviates significantly from the original loading path (grey line), even for the specimens under major-axis bending which have a relatively small slenderness ratio; and (2) the experimental loading paths terminate at points outside the boundary defined by the predicted *N-M* interaction diagram. The first observation above suggests that the slenderness effect, which generally leads to a decrease in load capacity, cannot be ignored for all the test specimens. The second observation is largely due to the fact that the ultimate axial strain of an eccentrically loaded specimen can be much larger than that of a corresponding concentrically loading specimen (see Table 6), noting that Model I, which is used in the section analysis, was developed based on concentric compression test results [i.e., a concentric-loading stress-strain model]. For the specimens under major-axis bending (Figures 13a, c, e), the load path outside the predicted *N-M* boundary is generally ascending with an increasing axial load, so the combined effect of the above two observations leads to a predicted peak load close to the experimental peak load (i.e., with differences within 12%, see Table 7). By contrast, for the specimens under minor-axis bending (Figures 13b, d, f), the load path outside the predicted *N-M* boundary is generally descending with a decreasing axial load, so the predicted load is generally smaller than the experimental peak load (by up to 27%, see Table 7) due to the slenderness effect. The different load paths of the specimens under major- and minor-axis bending are due to difference in both bending stiffness and degree of confinement non-uniformity, as explained in Section 3.2.2.

Apparently, to improve the accuracy of predictions for EFCRCCs under eccentric compression, the following two issues need to be addressed: (1) the slenderness effect; (2) the effect of strain gradient on the stress-strain behaviour of the confined concrete. In the next section, a theoretical model for EFCRCCs which takes into account the slenderness effect is presented, and various stress-strain models are considered to examine their effect on the prediction.

4.2 Theoretical Model Considering the Slenderness Effect

4.2.1 Method of analysis

A theoretical model was developed for EFCRCCs following the approach adopted by Jiang and Teng (2012) for slender FRP-confined circular RC columns. Jiang and Teng's (2012) model can generate accurate predictions for the axial load-lateral deflection response of columns, and their approach has been used in a number of subsequent studies (e.g., Hales et al., 2017; Saini and Prakash, 2021; Lin et al. 2020) on slender FRP-confined RC columns with different configurations.

Figure 14 illustrates the method of analysis for a column under equal load eccentricities at both ends (e.g., the specimens tested in this study). The column is equally divided into a desired number of segments with a length of ΔL. For a given cross-section of the column, a unique moment-curvature curve exists for a particular axial load N, so the axial load-moment-curvature (N-M-κ) relationship can be built through a series of conventional sectional analyses at various axial load levels. The lateral deflection at each grid point at a given load level can then be obtained in an iterative manner by using the (N-M-κ) relationship of the cross-section and the well-known numerical integration method of the column (Newmark 1943) as briefly summarised below.

By adopting the central difference equation, the relationship between the lateral deflection and the curvature can be expressed as:

$$\frac{\Delta_{(i+1)} - 2\Delta_{(i)} + \Delta_{(i-1)}}{\left(\Delta L\right)^2} = -\kappa_{(i)} \tag{2}$$

where $\Delta_{(i)}$ and $\kappa_{(i)}$ are the lateral deflection and the curvature at the ith grid point, respectively; i is the index of the grid point and $i = 1, 2, 3, \ldots, G$; $G - 1$ is the number of equal segments that the column is divided into (see Figure 14). Eq. 2 can be rewritten as:

$$\Delta_{(i+1)} = 2\Delta_{(i)} - \Delta_{(i-1)} - \kappa_{(i)}\left(\Delta L\right)^2 \tag{3}$$

An initial value for $\Delta_{(2)}$ needs to be first assumed to initiate the analysis; the assumed value can be any reasonably small value. Once the calculation reaches the other end of the column (point G), its lateral deflection needs to be examined to see whether it equals zero. If not, the value of $\Delta_{(2)}$ needs to be adjusted until the lateral deflection at point G equals zero (or is sufficiently close to zero). It should be noted that when calculating the bending moment at any grid point, the secondary bending moment (i.e., $N \times \Delta_{(i)}$) is taken into consideration. Readers may refer to Jiang and Teng (2012) for more details about the numerical integration process.

In the analysis, the stress-strain behaviour of the materials in EFCRCCs is considered in the same way as described in Section 4.1 for section analysis, except for the compressive stress-strain behaviour of the confined concrete, for which a few different stress-strain models are considered as discussed in the next subsection.

4.2.2 Results and discussions

Results using Liu et al.'s (2023) model (Model I) for confined concrete

The predictions of the theoretical analysis using Model I for the confined concrete are compared with the test results in Figures 15 and 16 in terms of the axial load-bending moment (N-M) curve and the axial load-lateral displacement curve, respectively. The predicted curves cease at the point where the axial strain at ECF reaches the ultimate value predicted by Model I. It is evident from Figure 15 that the theoretical model can accurately predict part of the trajectory of an N-M path including the slenderness effect but cannot reproduce the whole path to the experimental failure point. This is not a surprise as the ultimate axial strain predicted by Model I is for concentrically loaded columns and is thus significantly smaller than that for columns under eccentric compression. Nevertheless, it can be seen that the peak load of all the test specimens can be accurately predicted, as further illustrated in Figure 17. The peak load represents the load-carrying capacity of a column and is an important property for the design of EFCRCCs.

The observation from the Figure 16 is similar to that from Figure 15: the theoretical model can closely predict part of the axial load-lateral deflection curve, but the predicted curve generally terminates at a much smaller lateral deflection than the experimental curve. The predicted peak load and the corresponding bending moment, as well as the lateral deflection at the mid-height section of specimen, are listed in Table 8.

It is interesting to note that the errors in the prediction appear to be related to the bending direction of the specimen (see Table 8). Figure 18 shows the percentage error of the predicted peak load [i.e., (predicted value – experimental value) / experimental value]. It can be seen that the predicted peak load for a specimen under minor-axis bending is generally closer to the experimental value compared to that for a specimen under major-axis bending. For the latter, the prediction appears to be generally lower than the corresponding experimental value. This observation is believed to be largely due to the different characteristics of the curves of the two types of specimens (see Figure 16): those under major-axis bending have a curve that includes a generally ascending second branch while the corresponding curve for those under minor-axis bending includes a descending second branch. As Model I underestimates the ultimate axial strain of an eccentrically loaded column, the use of this model in the theoretical analysis leads to a predicted curve that is shorter than, and terminates at a point on the second branch of, the experimental curve. Furthermore, the non-uniform confinement over the cross-section (i.e., stronger near the major-axis vertices while weaker near the minor-axis vertices) to the concrete, as discussed in Section 3.2.2, might also contribute to the above differences in the predictions.

Figure 19 shows the percentage errors of predicted lateral displacements at the ultimate state Δ_u. It is evident that the prediction error of Δ_u increases with the normalised load eccentricity except for E20F80-S50 (Group B) which failed at an unusually low hoop rupture strain. The prediction error of Δ_u is again primarily due to the strain gradient effect which is not considered in Model I. As a result, similar to the ultimate axial strain, the percentage error of Δ_u is highly related to the sectional aspect ratio (a/b) and fibre orientations (Figure 19).

<u>Consideration of the strain gradient effect</u>

Lin and Teng (2019) proposed an eccentricity-dependent (EccD) stress-strain model for FRP-confined concrete in circular columns to account for the effect of strain gradient in eccentrically-loaded columns. The EccD stress-strain Model was developed based on the stiffness-based concentric-loading stress-strain model proposed by Lin et al. (2016), which is also the basis of Model I. Lin and Teng (2019) suggested that both E_2 and ε_{cu} are affected by the presence of strain gradient, and they proposed the following two formulas, respectively, to consider its effects:

$$E_{2,ecc} = E_{2,con}\left(1 - 0.0808\frac{E_{2,con}}{\left|E_{2,con}\right|}\frac{D}{c}\right), \quad \frac{D}{c} \leq 12.4 \tag{4}$$

$$\varepsilon_{cu,ecc} = \varepsilon_{cu,con}\left[1 + 0.263\frac{D}{c} + 0.0227\left(\frac{D}{c}\right)^2\right] \tag{5}$$

where $E_{2,ecc}$ is the slope of the second branch considering the strain gradient effect; $E_{2,con}$ is the slope of the second branch of the concentric-loading stress-strain model (i.e., E_2 in Model I); $\varepsilon_{cu,ecc}$ is the ultimate axial strain considering the strain gradient effect; $\varepsilon_{cu,con}$ is the ultimate axial strain of the concentric-loading stress-strain model (i.e., ε_{cu} in Model I); c is the height of neutral axis, which is determined from the ECF of the cross-section; D is the diameter of circular columns in Lin and Teng's (2019) model but is taken as the length of the axis on which the eccentricity e_i is located in the present study. According to Eqs. 4 and 5, with an increase in the height of the neutral axis, the slope of the second branch decreases while the ultimate axial strain increases.

By replacing E_2 and ε_{cu} with $E_{2,ecc}$ and $\varepsilon_{cu,ecc}$ in Model I, an EccD stress-strain model for the confined concrete in EFCRCCs can be obtained (hereafter referred to as Model IA). The predicted axial load-lateral displacement curves using Model IA are compared with the test results in Figure 20, while the key predicted results are summarised in Table 9. It can be seen that the predicted curves are longer than the corresponding curves predicted with the original Model I (Figure 16), but the predicted ultimate lateral displacements are still much smaller than the experimental values. This observation suggests that the formulae for the strain gradient effects on FRP-confined concrete in circular columns are not applicable to EFCRCCs. The underestimation of ultimate lateral displacement is again primarily due to the inaccurate prediction of ultimate axial strain of the confined concrete, as shown in Table 9. It can be seen in Table 9 that the predicted ultimate axial strains are closer to the test results for the specimens in Group A than for those in Groups B and C, suggesting that the strain gradient effect on the stress-strain behaviour of FRP-confined concrete may be related to the cross-section shape and fibre orientations. Despite the longer predicted curves (Figure 20), the use of the revised model does not seem to have a significant effect on the predicted peak loads (see Table 9 and Figure 20).

Further discussions

To further illustrate the effect of stress-strain model for the confined concrete on the predictions, the following two modification options were explored to Model I (Figure 21): (1) keeping E_2 from Model I and extending the second branch of the predicted stress-strain curve to the experimental ε_{cu} (hereafter referred to as Model IB); (2) keeping f'_{cc} from Model I and adopting the experimental ε_{cu} (i.e., E_2 is reduced accordingly) (hereafter referred to as Model IC). The predictions of the theoretical analysis with these two adjusted stress-strain models are compared with the test results in Figures 22-24. In making the predictions, the ε_{cu} value obtained by the LVDT at the ECF was used.

It is evident from Figures 22-24 that the predicted curves are now much longer, with ultimate lateral displacements being much closer to the experimental values, compared to the comparisons shown in Figures 16 and 20. The remaining differences between the predicted and experimental ultimate lateral displacements are believed to be due largely to the wide discrete cracks on the specimens during the late loading stage, which cannot be considered in the continuum mechanics-based theoretical analysis. It is also evident that the use of Model IB (i.e., keeping E_2 from Model I) generally leads to closer predictions than the use of Model IC (i.e., keeping f'_{cc} from Model I). It may be expected that the actual stress-strain path lies between the boundaries prescribed by the two modified stress-strain curves, as suggested by Lin and Teng (2019) for FRP-confined circular RC columns. The establishment of a more accurate stress-strain model for the confined concrete in eccentrically loaded EFCRCCs needs to be based on a reliable and sufficiently large database of the ultimate axial strain.

Nevertheless, the theoretical analysis based on Model I can already lead to reasonably accurate and conservative predictions for the peak load, as demonstrated above. Particularly, the predictions are considered accurate for the specimens with a descending second branch of axial load-displacement curve as the predicted curves generally go beyond the peak load point. For the specimens with an ascending second branch of axial load-displacement curve, the predictions are considered conservative as the predicted curves are generally shorter than the corresponding experimental curves. The trend of the second branch of a load-displacement curve depends on many factors, among which the slenderness ratio is an important one and needs to be further investigated in future.

5 CONCLUSIONS

This paper has presented the results of a series of eccentric compression tests on elliptical FRP tube-confined RC columns (EFCRCC). All the column specimens in the tests had the same height of 900 mm; the test variables included the fibre orientations in the FRP tube, sectional aspect ratio, load eccentricity and direction of bending. In addition, predictions from theoretical analysis, including sectional analysis as well as column analysis considering the second-order effect, are presented and compared with the test results. Based on the results and discussions presented in this study, the following conclusions can be drawn:

(1) The EFCRCCs tested in the present study under eccentric compression exhibited excellent structural performance, particularly excellent ductility. Within the parametric space examined in the study, the FRP tube provides effective confinement to the concrete in EFCRCCs.
(2) The EFCRCC specimens behaved quite differently when tested under load eccentricities in different directions. The specimens under major-axis bending had a load-displacement curve with a generally ascending second branch while the curves of those under minor-axis bending featured a descending second branch due to the relatively small bending stiffness of the latter.
(3) As expected, the axial load capacity of EFCRCCs decreases as the load eccentricity increases. This decrease appears to be more pronounced for specimens with a relatively high level of FRP confinement (e.g., with a relatively small sectional aspect ratio and/or a relatively large angle of fibre orientations).
(4) The ultimate axial strain of confined concrete in EFCRCCs increases with e_i, and this increases is highly related to the sectional aspect ratio and fibre orientations. The increase in the ultimate axial strain seems more pronounced for EFCRCCs with a larger sectional aspect ratio or confined by an FRP tube with a smaller fibre angle.
(5) The fibre orientations of the FRP tube may greatly affect the behaviour of EFCRCCs, including their failure mode. For EFCRCCs with fibres oriented more away from the hoop direction, failure may be controlled by FRP rupture on the tension side due to longitudinal tension instead of FRP rupture on the compression side due to the expansion of concrete.
(6) A theoretical slender column analysis based on the stress-strain model proposed by Liu et al., (2023) provides reasonably accurate and conservative predictions for the peak load of EFCRCCs under eccentric compression, although it generally underestimates the ultimate lateral displacement of EFCRCCs.

ACKNOWLEDGEMENTS

The authors are grateful for the financial support received from the Hong Kong Research Grants Council (Project No: PolyU 152217/15E) and the Hong Kong Innovation and Technology Fund (Project No: GHP/041/20GD). The experimental study was conducted at Guangdong University of Technology (GDUT). The authors are grateful for the support received from Dr Yong-Chang Guo, Mr Xiao-Dong Mo, Mr Zhen-Xiong Wang, Mr Jun-Jian Huang, Ms Chu-Ying Cui, Mr Dong-Ming Lai.

6 APPENDIX

<u>Model I (Liu et al., 2023)</u>

$$\sigma_c = \begin{cases} E_c\varepsilon_c - \dfrac{\left(E_c - E_2\right)^2}{4f_{co}^{'}}\varepsilon_c^2 & \left(0 \le \varepsilon_c < \varepsilon_t\right) \\ f_{co}^{'} + E_2\varepsilon_c \quad if\, \rho_{Ke} \ge 0.0113 & \left(\varepsilon_t \le \varepsilon_c \le \varepsilon_{cu}\right) \end{cases} \tag{A1}$$

$$\frac{E_2}{f_{co}^{'}} = 29.9\ln\left(\rho_K\right) + 134 \tag{A2}$$

$$\varepsilon_t = \frac{2f_{co}^{'}}{E_c - E_2} \tag{A3}$$

$$\rho_{Ke} = k_k\rho_K \tag{A4}$$

$$\rho_K = \frac{E_{FRP}t_f}{\left(f_{co}^{'} / \varepsilon_{co}\right)a} \tag{A5}$$

$$k_k = 0.095 \times \left(\frac{a}{b}\right)^2 - 0.860 \times \left(\frac{a}{b}\right) + 1.765 \tag{A6}$$

$$\frac{\varepsilon_{cu}}{\varepsilon_{co}} = 1.75 + 6.5 k_\varepsilon \rho_{Ke}^{0.8} \rho_\varepsilon^{1.45} \tag{A7}$$

$$\rho_\varepsilon = \frac{\varepsilon_{hu,circular}}{\varepsilon_{co}} \tag{A8}$$

$$k_\varepsilon = 0.19\left(\frac{a}{b}\right) + 0.81 \tag{A9}$$

where σ_c is the axial stress; ε_c is the axial strain; E_2 is the slope of the linear second portion; f'_{cc} is the compressive strength of confined concrete; f'_{co} is the compressive strength of unconfined concrete; E_c is the concrete elastic modulus, taken as $4730\sqrt{f'_{co}}$ (in MPa); ε_t is the transition strain between the parabolic first portion and the linear second portion; ε_{cu} is the axial strain of confined concrete at the ultimate state; ε_{co} is the strain at the compressive strength of unconfined concrete and is taken as 0.002; E_{FRP} is the hoop elastic modulus of FRP; t_f is the thickness of FRP tube; $\varepsilon_{hu,circular}$ is the hoop rupture strain of circular column, taken as 0.0192 and 0.0205 for specimens with an FRP tube with fibre orientation of ±80° and ±60°, respectively, according to Liu et al. (2023) where FRP tubes of the same batch as the ones in the present study were used; ρ_K is the confinement stiffness ratio; ρ_ε is the strain ratio; ρ_{Ke} is the effective confinement stiffness ratio; k_k is the modification factor for the equivalent confinement stiffness ratio; k_ε is a shape factor.

Axial stress-strain curves for concrete in concentrically loaded specimens

Figure A1 shows comparisons between experimental axial stress-strain curves of confined concrete in the concentrically loaded specimens of the present study (i.e., E15F80-S00; E20F80-S00; E15F60-S00) and the predicted curves from Model I. The axial strain was calculated using the average readings of the four LVDTs covering the 240 mm mid-height region (i.e., LVDTs 1-4). The axial stress was calculated by dividing the load taken by concrete by its area. The load taken by concrete was calculated by subtracting the loads taken by the steel rebars and the FRP tube from the total load on the column (Figure A2). The details of the calculation are the same as given in Liu et al. (2023).

Slenderness ratio of elliptical-section columns

For an elliptical cross-section, the radius of gyration for bending in the major axis direction r_x, or for bending in the minor axis r_y is calculated from:

$$A_g = \pi a b \tag{A10}$$

$$I_x = \frac{\pi a^3 b}{4} \tag{A11}$$

$$I_y = \frac{\pi a b^3}{4} \tag{A12}$$

$$r_x = \sqrt{\frac{I_x}{A_g}} = \frac{a}{2} \tag{A13}$$

$$r_y = \sqrt{\frac{I_y}{A_g}} = \frac{b}{2} \tag{A14}$$

where A_g = the gross cross-sectional area; I_x = the second-moment of area for bending in the major axis direction; I_y = the second moment of area for bending in the minor axis direction; The r (i.e., radius of gyration) value should be taken as r_x (i.e., $a/2$) for specimens under major-axis bending (i.e., e_i in the major-axis direction) or r_y (i.e., $b/2$) for specimens under minor-axis bending (i.e., e_i in the minor-axis direction). It should be noted that Eqs. A10-A14 do not account for differences in the elastic modulus for the constitutive materials of a composite cross-section. A transformed radius of gyration r_{tx} (or r_{ty}) can be calculated using the following equations for considering these differences in EFCRCCs (Siddiqui et al., 2014):

$$I_{tx} = I_x + (n_{es} - 1) I_{sx} + (n_{ef} - 1) I_{fx} \quad \text{(A15)}$$

$$A_t = A_g + (n_{es} - 1) A_s + (n_{ef} - 1) A_{frp} \quad \text{(A16)}$$

$$r_{tx} = \sqrt{\frac{I_{tx}}{A_t}} \quad \text{(A17)}$$

where A_s = the total cross-sectional area of the steel rebars; A_{frp} = the cross-sectional area of the FRP tube; I_{tx} = the transformed second moment of area for bending in the major axis direction; I_{sx} = the second moment of area of the steel rebars for bending in the major axis direction; I_{fx} = the second moment of area of the FRP tube for bending in the major axis direction; n_{es} = the ratio between the elastic modulus of the steel rebars and that of the concrete in EFCRCCs; n_{ef} = the ratio between the elastic modulus of the FRP tube and that of the concrete in EFCRCCs. It can be demonstrated that the consideration of the different elastic moduli of steel rebars, FRP tube and concrete in EFCRCCs using the above equations has little effect on the calculated results of the radius of gyration: for the specimens in the present study, the value of r_{tx} (or r_{ty}) is smaller than r_x (or r_y) by roughly 3.0%. The slenderness ratios calculated from Eqs. A10-A14 are thus used in the present study, and the value for each specimen is listed in Table 1.

7 REFERENCES

ACI. (2019). *Building code requirements for structural concrete and commentary*. *ACI 318-19*. Farmington Hills, MI, USA.

ASTM. (2014). *Standard test method for static modulus of elasticity and Poisson's ratio of concrete in compression*. *ASTM C469*. West Conshohocken, PA, USA.

ASTM. (2016a). *Standard test method for compressive strength of cylindrical concrete specimens*. *ASTM C39*. West Conshohocken, PA, USA.

ASTM. (2016b). *Standard Test Methods for Tension Testing of Metallic Materials*. *ASTM E8*. West Conshohocken, PA, USA.

Bisby, L., & Ranger, M. (2010). Axial–flexural interaction in circular FRP-confined reinforced concrete columns. *Construction and Building Materials*, *24*(9), 1672-1681.

Cao, Y.G., Jiang, C., & Wu, Y.F. (2016). Cross-sectional unification on the stress-strain model of concrete subjected to high passive confinement by fibre-reinforced polymer. Polymers, 8(5), 186.

Carrazedo, R., & de Hanai, J.B. (2017). Concrete prisms and cylinders wrapped by FRP loaded in compression with small eccentricities. *Journal of Composites for Construction*, *21*(4), 04016115.

Chen, G.P., Wang, Y.L., Yu, T., Wan, B.L., Zhang, B., & Liu, Q. (2021). Behaviour and design-oriented model for elliptical FRP-confined concrete under axial compression. *Engineering Structures*, *249*, 113387.

Chen, G.P., Wang, Y.L., Yu, T., Zhang, B., & Zhang, Y.N. (2023). Cyclically loaded elliptical FRP-confined concrete: behavioral characteristics and modeling. *Engineering Structures*, 285, 116044.

Chen, G., Wang, Y., Yu, T., Zhang, B., & Han, B. (2022). Elliptical FRP–concrete–steel double-skin tubular columns: axial behavior, interaction mechanism, and modeling. *Journal of Composites for Construction*, 26(6), 04022078.

Claeson, C., & Gylltoft, K. (1998). Slender high-strength concrete columns subjected to eccentric loading. *Journal of Structural Engineering*, *124*(3), 233-240.

Csuka, B., & Kollár, L.P. (2011). FRP-confined circular columns subjected to eccentric loading. *Journal of Reinforced Plastics and Composites*, *30*(14), 1167-1178.

BSI. (2004). *Eurocode 2: Design of concrete structures: Part 1-1: General rules and rules for buildings*. British Standards Institution.

GB. (2020). *Technical standard for fibre reinforced polymer (FRP) in construction*. *GB 50608*. China Planning Press, Beijing.

GB/T. (2005). *Fibre-reinforced thermosetting plastic composites pipe-determination for longitudinal compressive properties*. *GB/T 5350*. Standardization Administration of the PRC, Beijing.

Hadi, M. (2006). Behaviour of FRP wrapped normal strength concrete columns under eccentric loading. *Composite Structures*, *72*(4), 503-511.

Hadi, M.N. (2007a). Behaviour of FRP strengthened concrete columns under eccentric compression loading. *Composite Structures*, *77*(1), 92-96.

Hadi, M.N. (2007b). The behaviour of FRP wrapped HSC columns under different eccentric loads. *Composite Structures*, *78*(4), 560-566.

Hadi, M.N., & Widiarsa, I.B.R. (2012). Axial and flexural performance of square RC columns wrapped with CFRP under eccentric loading. *Journal of Composites for Construction*, *16*(6), 640-649.

Hain, A., Motaref, S., & Zaghi, A.E. (2019). Influence of fiber orientation and shell thickness on the axial compressive behavior of concrete-filled fiber-reinforced polymer tubes. *Construction and Building Materials*, *220*, 353-363.

Hales, T.A., Pantelides, C.P., & Reaveley, L.D. (2017). Analytical buckling model for slender FRP-reinforced concrete columns. *Composite Structures*, *176*, 33-42.Jiang, C., & Wu, Y.F. (2020). Axial strength of eccentrically loaded FRP-confined short concrete columns. *Polymers*, *12*(6), 1261.

Jiang, T., & Teng, J.G. (2012). Theoretical model for slender FRP-confined circular RC columns. *Construction and Building Materials*, *32*, 66-76.

Khorramian, K., & Sadeghian, P. (2021). Slender RC Columns Strengthened with a Novel Hybrid Strengthening System of External Longitudinal and Transverse FRPs. *Journal of Structural Engineering*, *147*(10), 04021154.

Popovics S. (1998) *Strength and Related Properties of Concrete: A Quantitative Approach*, John Wiley & Sons, Inc., New York.

Lin, G., & Teng, J.G. (2019). Stress-strain model for FRP-confined concrete in eccentrically loaded circular columns. *Journal of Composites for Construction*, *23*(3), 04019017.

Lin, G., Yu, T., & Teng, J.G. (2016). Design-oriented stress–strain model for concrete under combined FRP-steel confinement. *Journal of Composites for Construction*, *20*(4), 04015084.

Lin, G., & Teng, J.G. (2017). Three-dimensional finite-element analysis of FRP-confined circular concrete columns under eccentric loading. *Journal of Composites for Construction*, *21*(4), 04017003.

Liu, K.C. (2023). *Behaviour and modelling of elliptical FRP tube-confined reinforced concrete columns*, PhD dissertation, The Hong Kong Polytechnic University.

Liu, K.C., Jiang, C., Yu, T., & Teng, J.G. (2023). Compressive behaviour of elliptical FRP tube-confined concrete columns. *Composite Structures*, 303, 116301.

Lin, G., Zeng, J.J., Teng, J.G., & Li, L.J. (2020). Behavior of large-scale FRP-confined rectangular RC columns under eccentric compression. *Engineering Structures*, 216, 110759.

Mirmiran, A., Shahawy, M., & Beitleman, T. (2001). Slenderness limit for hybrid FRP-concrete columns. *Journal of Composites for Construction*, *5*(1), 26-34.

Ozbakkaloglu, T., & Saatcioglu, M. (2006). Seismic behavior of high-strength concrete columns confined by fiber-reinforced polymer tubes. *Journal of Composites for Construction*, 10(6), 538-549.

Parvin, A., & Wang, W. (2001). Behavior of FRP jacketed concrete columns under eccentric loading. *Journal of Composites for Construction*, *5*(3), 146-152.

Ram, B. (2012). *Engineering Mathematics, Volume I, Second Edition*. Pearson India.

Rocca, S., Galati, N., & Nanni, A. (2009). Interaction diagram methodology for design of FRP-confined reinforced concrete columns. *Construction and Building Materials*, 23(4), 1508-1520.

Rejab, M. R. M., Kadirgama, K., Noor, M. M., Sani, M. S. M., & Daud, R. (2008). Modification and testing of four axes filament winding machine. In *International Conference on Science & Technology: Application in Industry & Education*.

Saafi, M., Toutanji, H., & Li, Z. (1999). Behavior of concrete columns confined with fiber reinforced polymer tubes. *Materials Journal*, 96(4), 500-509.

Saini, A., & Prakash, S.S. (2021). Analytical study on the effectiveness of hybrid FRP strengthening on behaviour of slender reinforced concrete square columns. *Structures*, 33, 4218-4242.

Shaikh, F.U.A., & Alishahi, R. (2019). Behaviour of CFRP wrapped RC square columns under eccentric compressive loading. *Structures*, 20, 309-323.

Siddiqui, N.A., Alsayed, S.H., Al-Salloum, Y.A., Iqbal, R.A., & Abbas, H. (2014). Experimental investigation of slender circular RC columns strengthened with FRP composites. *Construction and Building Materials*, *69*, 323-334.

Song, X.B., Gu, X.L., Li, Y.P., Chen, T., & Zhang, W.P. (2013). Mechanical behavior of FRP-strengthened concrete columns subjected to concentric and eccentric compression loading. *Journal of Composites for Construction*, *17*(3), 336-346.

Teng, J.G., & Lam, L. (2002). Compressive behavior of carbon fiber reinforced polymer-confined concrete in elliptical columns. *Journal of Structural Engineering*, 128(12), 1535-1543.

Teng, J.G., Wu, J.Y., Casalboni, S., Xiao, Q.G., & Zhao, Y. (2016). Behavior and modeling of fibre-reinforced polymer-confined concrete in elliptical columns. *Advances in Structural Engineering*, *19*(9), 1359-1378.

Teng, J.G., Xie, P., Wang, Z.H., & Liu, K.C. (2023). *A novel test method for the determination of hoop elastic modulus and Poisson's ratio of FRP tubes*. (Chinese Patent CN 113281166 B). National Intellectual Property Administration, PRC

Tijani, I.A., Jiang, C., Lim, C., & Wu, Y.F. (2022). Eccentrically Loaded Concrete under Nonuniform Passive Confinement. *Journal of Structural Engineering*, *148*(1), 04021247.

Vincent, T., & Ozbakkaloglu, T. (2013). Influence of fibre orientation and specimen end condition on axial compressive behaviour of FRP-confined concrete. *Construction and Building Materials*, 47, 814-826.Xing, L., Lin, G., & Chen, J.F. (2020). Behavior of FRP-confined circular RC columns under eccentric compression. *Journal of Composites for Construction*, *24*(4), 04020030.

Yu, T., & Teng, J.G. (2011). Design of concrete-filled FRP tubular columns: provisions in the Chinese technical code for infrastructure application of FRP composites. *Journal of Composites for Construction*, 15(3), 451-461.

Zhang, B., Feng, G.S., Wang, Y.L., Lai, C.C., Wang, C.C., & Hu, X.M. (2020). Elliptical FRP-Concrete-Steel Double-Skin Tubular Columns under Monotonic Axial Compression. *Advances in Polymer Technology*, 2020(1), 7573848.

Zhang, B., Zhou, C., Wang, C., Li, Y., Gao, Y., & Zheng, H. (2023). Seismic behavior and modeling of elliptical concrete-filled FRP tubes with longitudinal steel rebars under lateral cyclic load and vertical constant load. *Thin-Walled Structures*, 188, 110815.

Table 1 Details of specimens

No.	Specimen	Aspect Ratio	Major axis length 2a (mm)	Minor axis length 2b (mm)	Height (mm)	Slenderness ratio λ	FRP tube	
							Tube thickness (mm)	Number of fibre layers/ Fibre orientations
Group A	E15F80-S00	1.5	301.2	200.4	902.5	9.0	2.82	6/±80°
	E15F80-S25		301.7	200.1	894.7	11.9	2.90	
	E15F80-S50		300.5	200.5	900.2	12.0	2.40	
	E15F80-S120		301.0	201.8	897.0	11.9	2.41	
	E15F80-W25		304.0	203.0	894.2	17.6	2.70	
	E15F80-W50		296.3	197.2	891.5	18.1	2.23	
Group B	E20F80-S00	2.0	301.2	155.0	899.9	11.6	2.41	
	E20F80-S25		302.9	155.5	900.8	11.9	2.63	
	E20F80-S50		301.6	155.7	906.0	12.0	2.78	
	E20F80-S120		301.1	154.7	901.2	12.0	2.58	
	E20F80-W25		299.9	155.2	904.9	23.3	2.81	
	E20F80-W50		299.9	154.5	901.5	23.3	2.41	
Group C	E15F60-S00	1.5	302.2	202.0	891.5	8.8	3.06	6/±60°
	E15F60-S25		300.5	202.6	900.0	12.0	2.90	
	E15F60-S50		305.1	204.4	911.5	12.0	3.51	
	E15F60-S120		301.2	201.7	907.8	12.1	3.01	
	E15F60-W25		304.2	203.4	909.5	17.9	3.24	
	E15F60-W50		302.2	202.6	909.5	18.0	3.06	

Table 2 Mix proportions of concrete

Coarse aggregate (kg/m^3)	Fine aggregate (kg/m^3)	Cement (kg/m^3)	Water (kg/m^3)	Water reducer (kg/m^3)
1072	760	343	175	N.A.

Table 3 Properties of concrete

	Compressive strength f'_{co} (MPa)	Average f'_{co} (MPa)	Elastic modulus E_c (GPa)	Average E_c (GPa)	ε_{co} (%)	Average ε_{co} (%)	Poisson's ratio v	Average v
28th day	40.3	41.2	34.3	34.2	0.211	0.218	0.194	0.185
	41.5		34.5		0.225		0.179	
	41.8		33.7		0.219		0.182	
42nd day	41.9	43.2	35.4	34.6	0.234	0.228	0.197	0.186
	44.8		35.4		0.232		0.176	
	42.8		33.0		0.218		0.184	

Table 4 Properties of FRP tubes

Fibre orientations	Curved coupon test		FRP ring test			
	Thickness $t_{FRP,h}$ (mm)	$E_{FRP,h}$ (GPa)	Thickness $t_{FRP,a}$ (mm)	$E_{FRP,a}$ (GPa)	Peak stress (MPa)	Poisson's ratio
±80°	3.30	38.1	2.84	10.6	70.5	0.093
±60°	3.04	15.6	3.42	14.9	68.9	0.470

Table 5 Properties of steel rebars

Diameter	Ref. no.	Yield stress f_y (MPa)	Average f_y (MPa)	Tensile strength f_{su} (MPa)	Average f_{su} (MPa)	Elastic moduli E_s (GPa)	Average E_s (GPa)
Φ16	1	433.5	432.7	615.7	618.1	198.6	199.4
	2	436.6		618.8		193.8	
	3	427.2		615.7		207.8	
	4	433.5		622.0		192.6	
Φ18	1	451.7	441.2	613.1	605.0	209.6	202.9
	2	431.9		595.7		196.6	
	3	439.3		608.1		201.5	
	4	441.8		603.1		204.0	

Table 6 Key column test results

Specimen	At the peak load					At the ultimate state						Rupture location (C/T)[a]
	F_{max} (kN)	M_{Fmax} (kN·m)			Δ_{Fmax} (mm)	F_u (kN)	Δ_u (mm)	ε_{cu} (%)[e] (LVDT)	$\varepsilon_{hu,max}$ (%)	SG with $\varepsilon_{hu,max}$	Non-functional hoop SGs[f]	
		M_i	M_Δ	Total								
E15F80-S00	3649.8	-[c]				3649.8	-	2.06	1.11[b]	H2	H1, H13	C
E15F80-S25	2820.3	70.5	78.6	149.1	27.9	2820.3	27.9	5.56	1.61	H15	H1, H2, H16	C
E15F80-S50	2058.0	102.9	69.6	172.5	33.8	2058.0	33.8	6.08	1.86	H1	-	C
E15F80-S120	1027.0	123.2	52.6	175.8	51.7	1019.1	55.2	8.14	-	-	All	C
E15F80-W25	2042.2	51.0	43.4	94.4	21.2	1757.8	44.6	7.00	1.59	H13	H1, H10, H14, H16	C
E15F80-W50	1437.8	71.9	15.2	87.1	10.6	1042.8	53.1	6.48	-	-	All	C
E20F80-S00	2223.9	-				2223.9	-	1.35	1.11[b]	H10	H7, H8, H9	C
E20F80-S25	1955.3	48.9	59.9	108.8	30.6	1951.3	32.5	6.34	1.69	H15	H1, H2, H4, H14, H16	C
E20F80-S50	1477.3	73.9	36.2	110.1	24.5	1477.3	24.5	4.40	1.09	H15	H1, H2, H16	C
E20F80-S120	809.8	97.2	35.9	133.1	44.3	794.0	60.9	8.14	1.29	H14	H1, H2, H4-8, H15-16	C
E20F80-W25	1208.7	30.2	11.1	41.3	9.2	596.5	77.8	7.58	-	-	All	C
E20F80-W50	794.0	39.7	7.6	47.3	9.6	395.0	100.6	8.87	-	-	All	C
E15F60-S00	2618.9	-				2532.0	-	1.21	1.45	H5	-	C
E15F60-S25	2216.0	55.4	40.1	95.5	18.1	2176.5	33.3	6.91	4.14	H2	H1, H3	C
E15F60-S50	1797.3	89.9	42.5	132.4	23.7	1730.1	48.3	9.07	-	-	All	C
E15F60-S120[d]	-	-	-	-	-	-	-	-	-	-	-	-
E15F60-W25	1844.7	46.1	9.1	55.2	4.92	1193.0	75.8	10.0	-	-	All	T
E15F60-W50	1331.2	66.6	15.1	81.7	11.4	912.5	72.7	9.51	-	-	All	T

Notes:

a. The letter “C” denotes “the compression side”; the letter “T” denotes “the tension side”.
b. The measured hoop strain is much smaller than expected because rupture did not occur at the mid-height section where the strain gauges were installed.
c. The symbol “-” denotes that the relevant result is not available.
d. Specimen E15E2-SS-120 failed prematurely at the beginning of the test due to the fracture of weld between the steel rebars and the upper steel plate; the results of this specimen are thus not available.
e. For eccentrically loaded columns, the axial strain at the extreme compression fibre (ECF) at the mid-height section is reported here; for concentrically loaded columns, the average axial strain over the cross-section is reported here.
f. The numbering of strain gauges is given in Figure 4.

Table 7 Predicted peak loads and corresponding bending moments of columns from section analysis

Group	Specimen	$F_{max,exp}$ (kN)	$F_{max,pre}$ (kN)	$F_{max,pre}/F_{max,exp}$	$M_{Fmax,exp}$ (kN·m)	$M_{Fmax,pre}$ (kN·m)	$M_{Fmax,pre}/ M_{Fmax,exp}$
Group A	E15F80-S25	2820.3	2752.8	0.98	149.1	68.8	0.46
	E15F80-S50	2058.0	2179.0	1.06	172.5	109.6	0.64
	E15F80-S120	1027.0	1147.7	1.12	175.8	137.8	0.78
	E15F80-W25	2042.2	2461.5	1.21	94.4	61.4	0.65
	E15F80-W50	1437.8	1827.6	1.27	87.1	92.0	1.06
Group B	E20F80-S25	1955.3	1861.5	0.95	108.8	46.7	0.43
	E20F80-S50	1477.3	1493.3	1.01	110.7	74.4	0.67
	E20F80-S120	809.8	810.3	1.00	133.1	97.6	0.73
	E20F80-W25	1208.7	1462.2	1.21	41.3	36.9	0.89
	E20F80-W50	794.0	960.4	1.21	47.3	48.1	1.02
Group C	E15F60-S25	2216.0	2125.1	0.96	95.5	53.3	0.56
	E15F60-S50	1797.3	1717.9	0.96	132.4	86.2	0.65
	E15F60-W25	1844.7	1902.5	1.03	55.2	48.0	0.87
	E15F60-W50	1331.2	1461.5	1.10	81.7	73.7	0.90
Average				1.08			0.74

Note: $F_{max,exp}$ and $M_{Fmax,exp}$ = experimental peak load and corresponding moment; $F_{max,pre}$ and $M_{Fmax,pre}$ = predicted peak load and corresponding moment.

Table 8 Comparisons between column test results and theoretical predictions with the use of Model I

Group	Specimen	$F_{max,exp}$ (kN)	$F_{max,pre}$ (kN)	$F_{max,pre}$/ $F_{max,exp}$	$M_{Fmax,exp}$ (kN·m)	$M_{Fmax,pre}$ (kN·m)	$M_{Fmax,pre}$/ $M_{Fmax,exp}$	$\Delta_{u,exp}$ (mm)	$\Delta_{u,pre}$ (mm)	$\Delta_{u,pre}$/ $\Delta_{u,exp}$
Group A	E15F80-S25	2820.3	2491.1	0.88	149.1	89.4	0.60	27.9	10.9	0.39
	E15F80-S50	2058.0	1966.8	0.96	172.5	122.7	0.71	33.8	12.4	0.37
	E15F80-S120	1027.0	1001.9	0.98	176.8	137.0	0.77	55.2	16.7	0.30
	E15F80-W25	2042.2	2051.2	1.00	94.4	84.3	0.89	44.6	16.1	0.36
	E15F80-W50	1437.8	1456.8	1.01	87.1	85.7	0.98	53.1	18.4	0.35
Group B	E20F80-S25	1955.3	1738.8	0.89	108.8	57.2	0.53	32.5	7.9	0.24
	E20F80-S50	1477.3	1387.0	0.94	110.7	81.6	0.74	24.5	8.9	0.36
	E20F80-S120	809.8	748.1	0.92	133.1	98.8	0.74	60.9	11.2	0.18
	E20F80-W25	1208.7	1221.0	1.01	41.3	37.3	0.90	77.8	14.5	0.19
	E20F80-W50	794.0	799.3	1.01	47.3	45.7	0.97	100.6	15.2	0.15
Group C	E15F60-S25	2216.0	2005.3	0.90	95.5	58.7	0.61	33.3	4.7	0.14
	E15F60-S50	1797.3	1667.1	0.93	132.4	87.9	0.66	48.3	4.6	0.10
	E15F60-W25	1844.7	1823.8	0.99	55.2	53.4	0.97	75.8	6.5	0.09
	E15F60-W50	1331.2	1363.2	1.02	81.7	76.7	0.94	72.7	6.3	0.09
Average				0.96			0.79			0.24

Note: $F_{max,exp}$ and $M_{Fmax,exp}$ = experimental peak load and corresponding moment; $F_{max,pre}$ and $M_{Fmax,pre}$ = predicted peak load and corresponding moment; $\Delta_{u,exp}$ and $\Delta_{u,pre}$ = experimental and predicted lateral displacements of the mid-height section at the ultimate state.

Table 9 Comparisons between column test results and theoretical predictions with the use of Model IA

Group	Specimen	$F_{max,exp}$ (kN)	$\Delta_{u,exp}$ (mm)	$\varepsilon_{cu,exp}$	Model IA [adopting Lin and Teng's (2019) method]					
					$F_{max,pre}$ (kN)	$F_{max,pre}$/ $F_{max,exp}$	$\Delta_{u,pre}$ (mm)	$\Delta_{u,pre}$/ $\Delta_{u,exp}$	$\varepsilon_{cu,pre}$	$\varepsilon_{cu,pre}$/ $\varepsilon_{cu,exp}$
Group A	E15F80-S25	2820.3	27.9	0.056	2527.7	0.90	15.1	0.54	0.0388	0.69
	E15F80-S50	2058.0	33.8	0.061	2011.5	0.98	17.5	0.51	0.0398	0.65
	E15F80-S120	1027.0	55.2	0.081	989.9	0.96	27.2	0.49	0.0462	0.57
	E15F80-W25	2042.2	44.6	0.070	2018.3	0.99	22.2	0.50	0.0395	0.56
	E15F80-W50	1437.8	53.1	0.065	1438.4	1.00	29.2	0.55	0.0451	0.69
Group B	E20F80-S25	1955.3	32.5	0.063	1735.7	0.89	10.7	0.33	0.0291	0.46
	E20F80-S50	1477.3	24.5	0.044	1388.6	0.94	12.4	0.51	0.0300	0.68
	E20F80-S120	809.8	60.9	0.081	744.9	0.92	18.0	0.30	0.0345	0.43
	E20F80-W25	1208.7	77.8	0.076	1215.2	1.01	20.0	0.26	0.0320	0.42
	E20F80-W50	794.0	100.6	0.089	795.3	1.00	24.1	0.24	0.0346	0.39
Group C	E15F60-S25	2216.0	33.3	0.069	1989.7	0.90	5.9	0.18	0.0193	0.28
	E15F60-S50	1797.3	48.3	0.091	1666.2	0.93	5.7	0.12	0.0202	0.22
	E15F60-W25	1844.7	75.8	0.100	1823.2	0.99	7.9	0.10	0.0195	0.20
	E15F60-W50	1331.2	72.7	0.095	1360.7	1.02	7.7	0.11	0.0204	0.21
Average					-	0.96	-	0.34	-	0.46

Note: $F_{max,exp}$ and $F_{max,pre}$ = experimental and predicted peak loads, respectively; $\Delta_{u,exp}$ and $\Delta_{u,pre}$ = experimental and predicted lateral displacements of the mid-height section at the ultimate state, respectively; $\varepsilon_{cu,exp}$ and $\varepsilon_{cu,pre}$ = experimental and predicted axial strains at ECF (measured by LVDT) at the ultimate state, respectively.

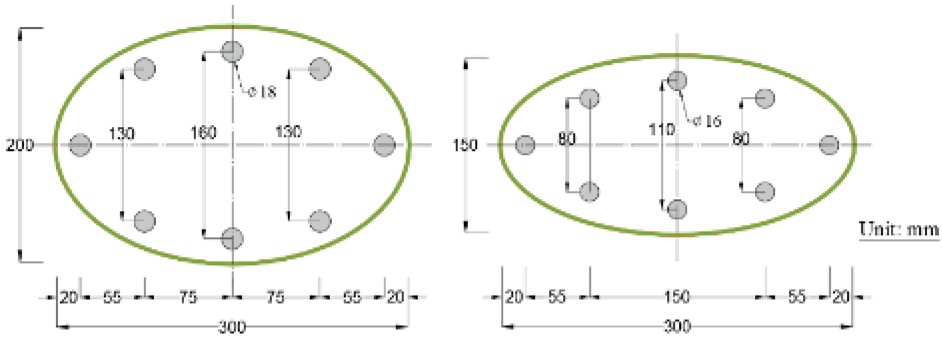

(a) Cross-section with an aspect ratio of 1.5 (b) Cross-section with an aspect ratio of 2.0

Figure 1 Layouts of longitudinal steel reinforcement

(a) Welding longitudinal rebars to the bottom steel plate

(b) Placing the FRP tube and the top steel plate

(c) Welding the longitudinal rebars to the top steel plate

(d) Fixing the FRP tube and sealing the joints

(e) Casting the concrete

Figure 2 Preparation of column specimens

(a)

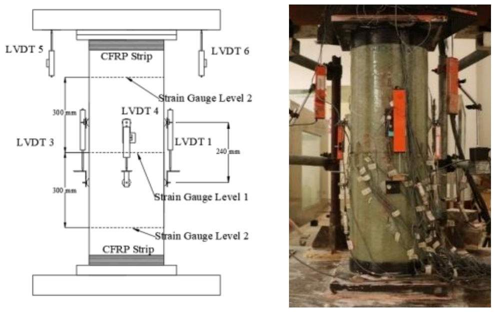

(b)

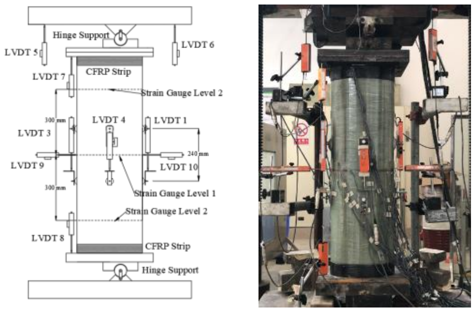

Figure 3 Test set-ups: (a) concentrically loaded columns; (b) eccentrically loaded columns

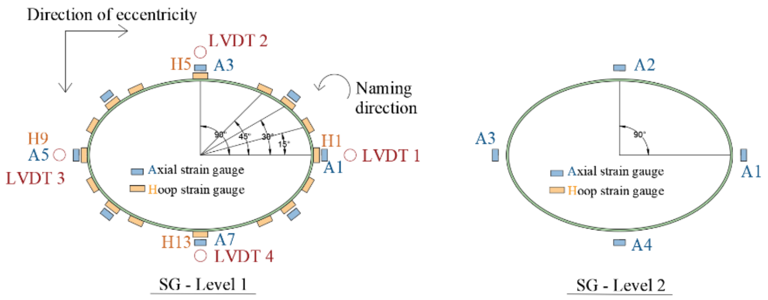

(a)

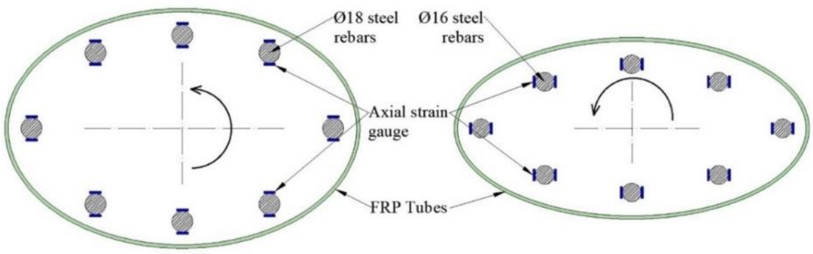

(b)

Figure 4 Layouts of strain gauges and LVDTs: (a) strain gauges and LVDTs on the FRP tube; (b) strain gauges on the steel rebars

(a) E15F80-S00

(b) E20F80-S00

(c) E15F60-S00

Figure 5 Failure modes of concentrically loaded columns

(a) Specimens with e_i = 25 mm on the major axis

(b) Specimens with e_i = 50 mm on the major axis

(c) Specimens with e_i = 120 mm on the major axis

(d) Specimens with e_i = 25 mm on the minor axis

(e) Specimens with e_i = 50 mm on the minor axis

Figure 6 Failure modes of eccentrically loaded columns

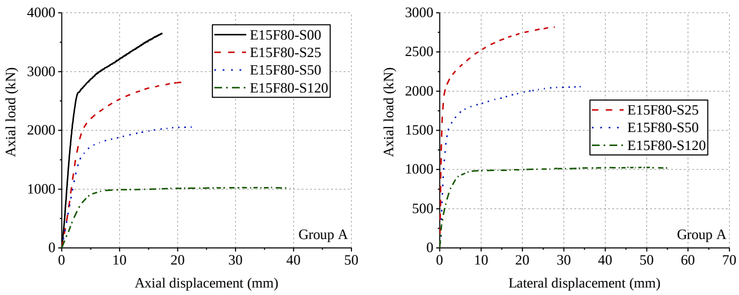

(a) Aspect ratio = 1.5, fibre orientation = 80°

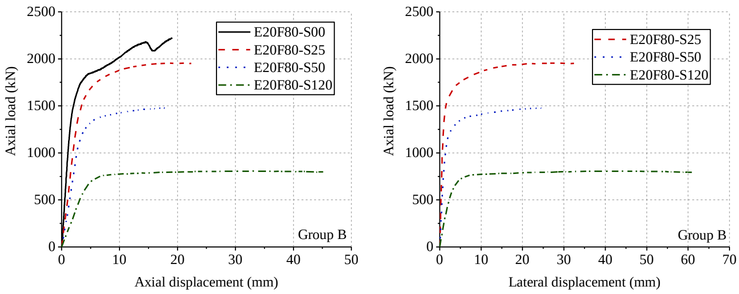

(b) Aspect ratio = 2.0, fibre orientation = 80°

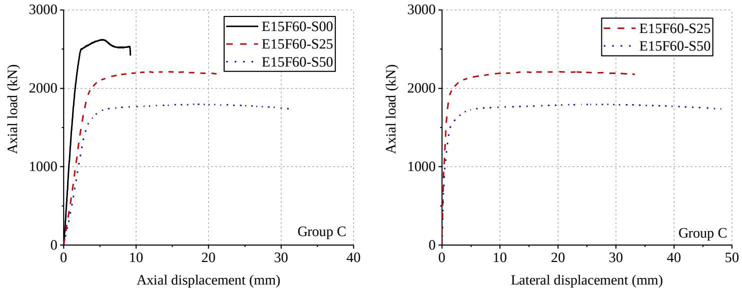

(c) Aspect ratio = 1.5, fibre orientation = 60°

Figure 7 Effect of initial load eccentricity (e_i) on the load-displacement behaviour: columns under major-axis bending

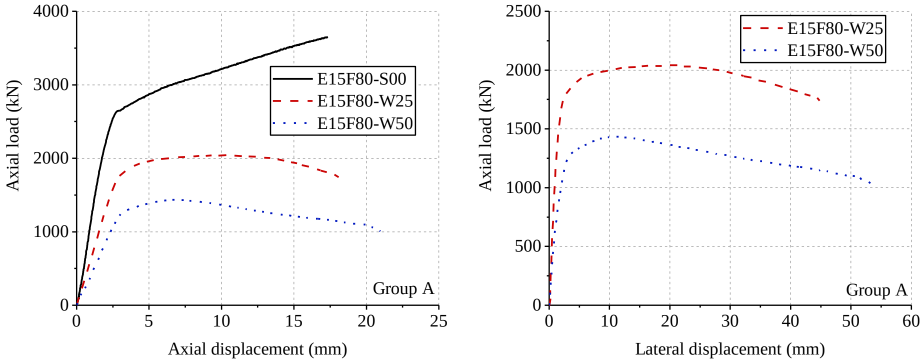

(a) Aspect ratio = 1.5, fibre orientation = 80°

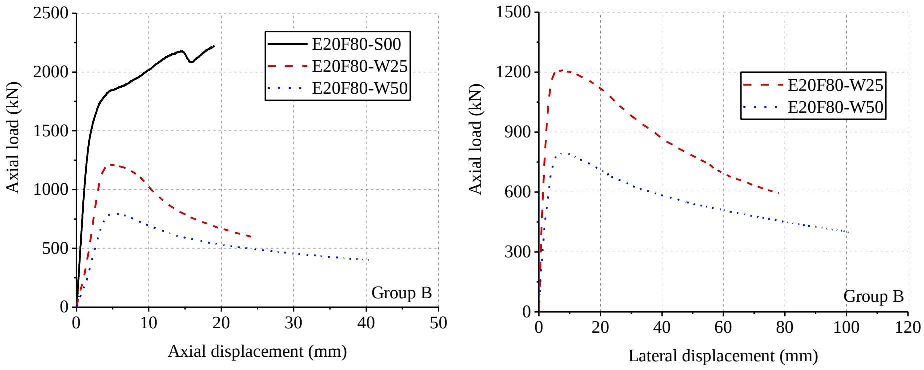

(b) Aspect ratio = 2.0, fibre orientation = 80°

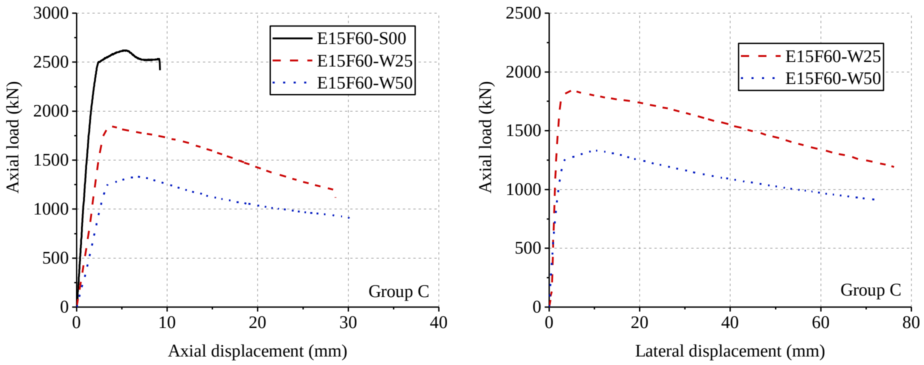

(c) Aspect ratio = 1.5, fibre orientation = 60°

Figure 8 Effect of initial load eccentricity (e_i) on the load-displacement behaviour: columns under minor-axis bending

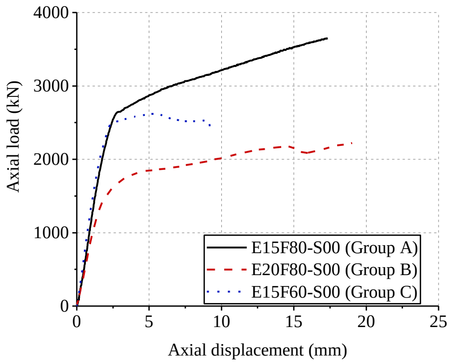

(a) e_i = 0 mm (major-axis direction)

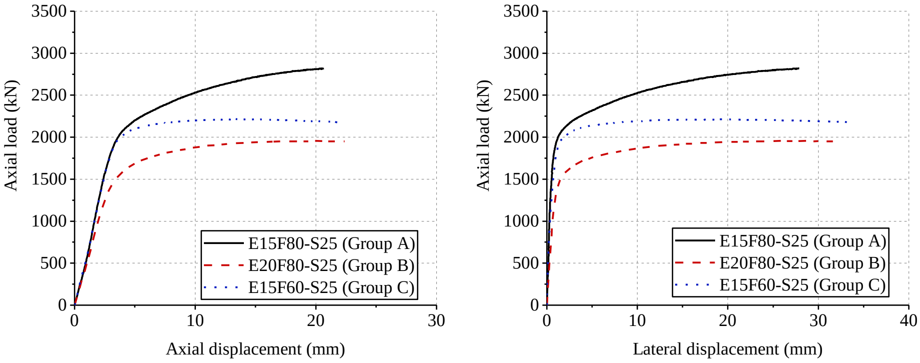

(b) e_i = 25 mm (major-axis direction)

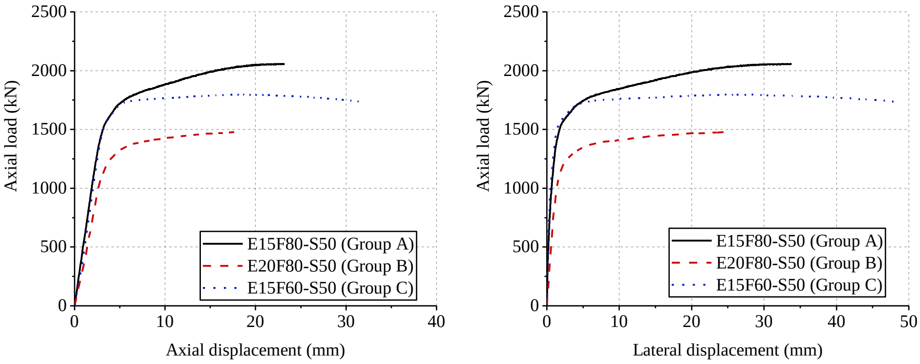

(c) e_i = 50 mm (major-axis direction)

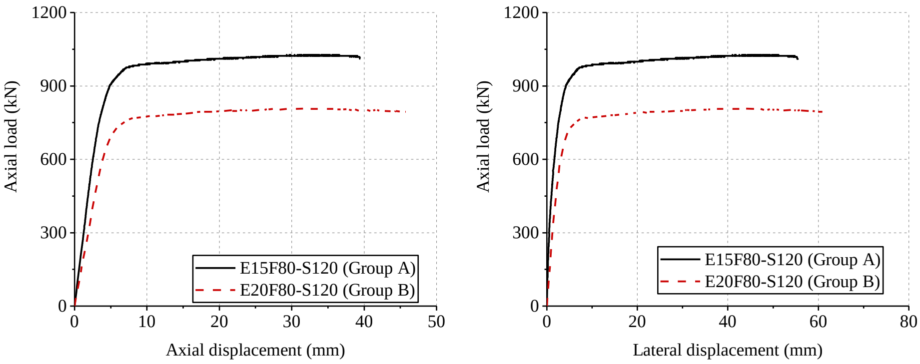

(d) e_i = 120 mm (major-axis direction)

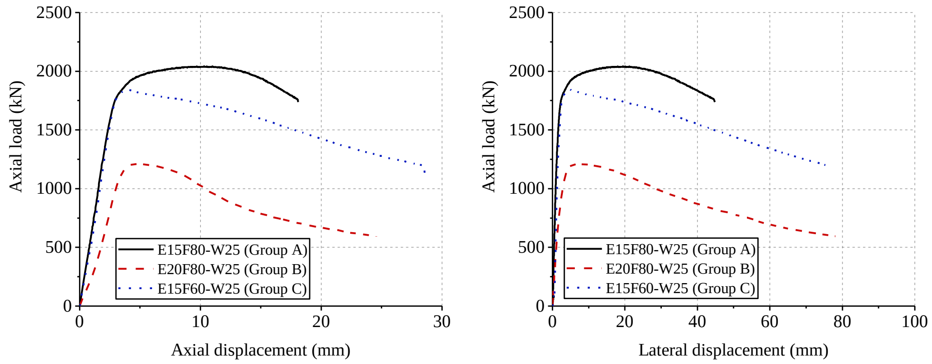

(e) e_i = 25 mm (minor-axis direction)

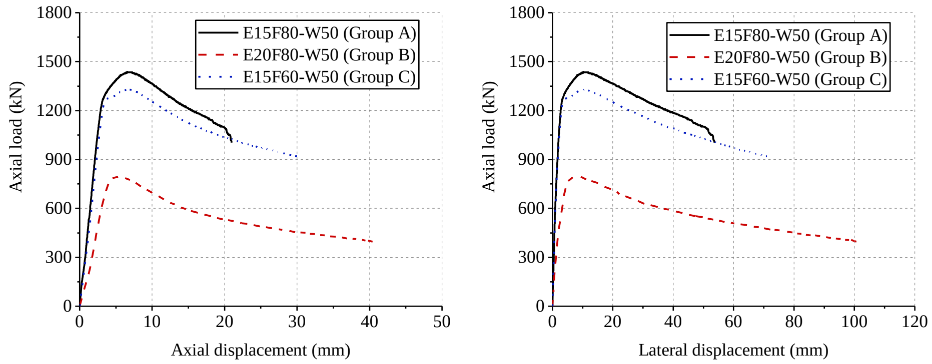

(f) e_i = 50 mm (minor-axis direction)

Figure 9 Effects of aspect ratio and fibre orientations on the load-displacement behaviour

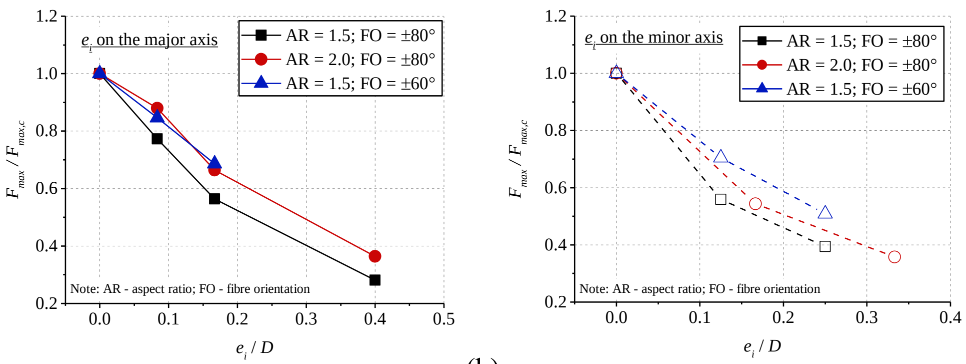

(a) (b)

Figure 10 Normalized e_i versus normalised peak load (F_{max} / $F_{max,c}$)

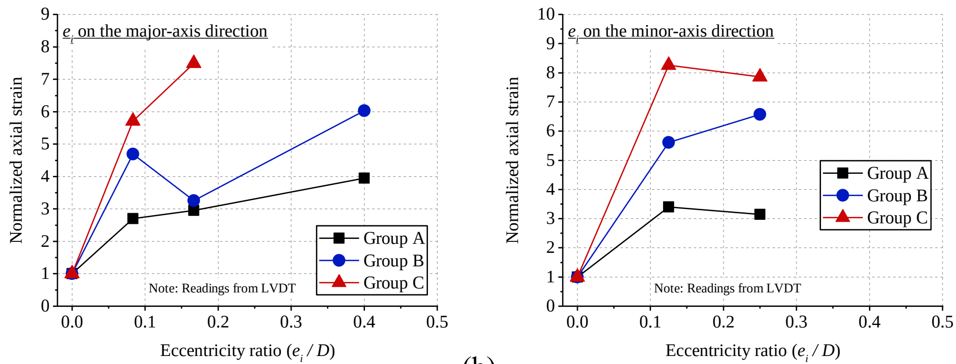

(a) (b)

Figure 11 Correlation between the eccentricity ratio and the strain capacity of confined concrete

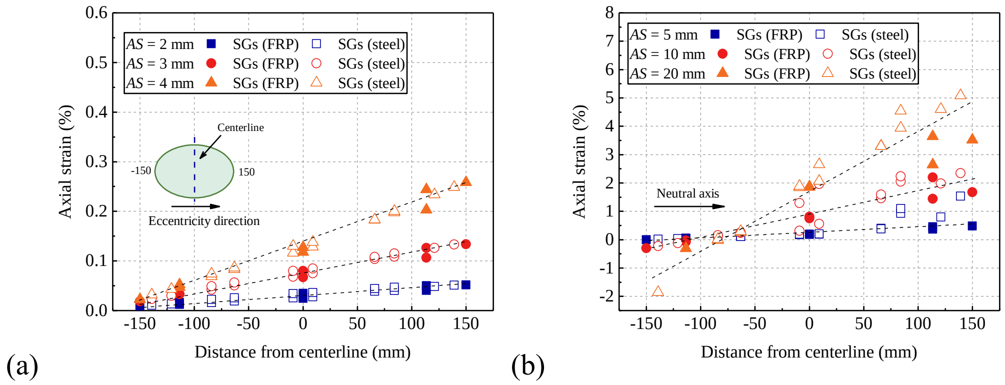

Figure 12 Typical axial strain distributions over the mid-height cross-section (for Specimen E15F80-S25 with an ultimate axial shortening of 20.7 mm)

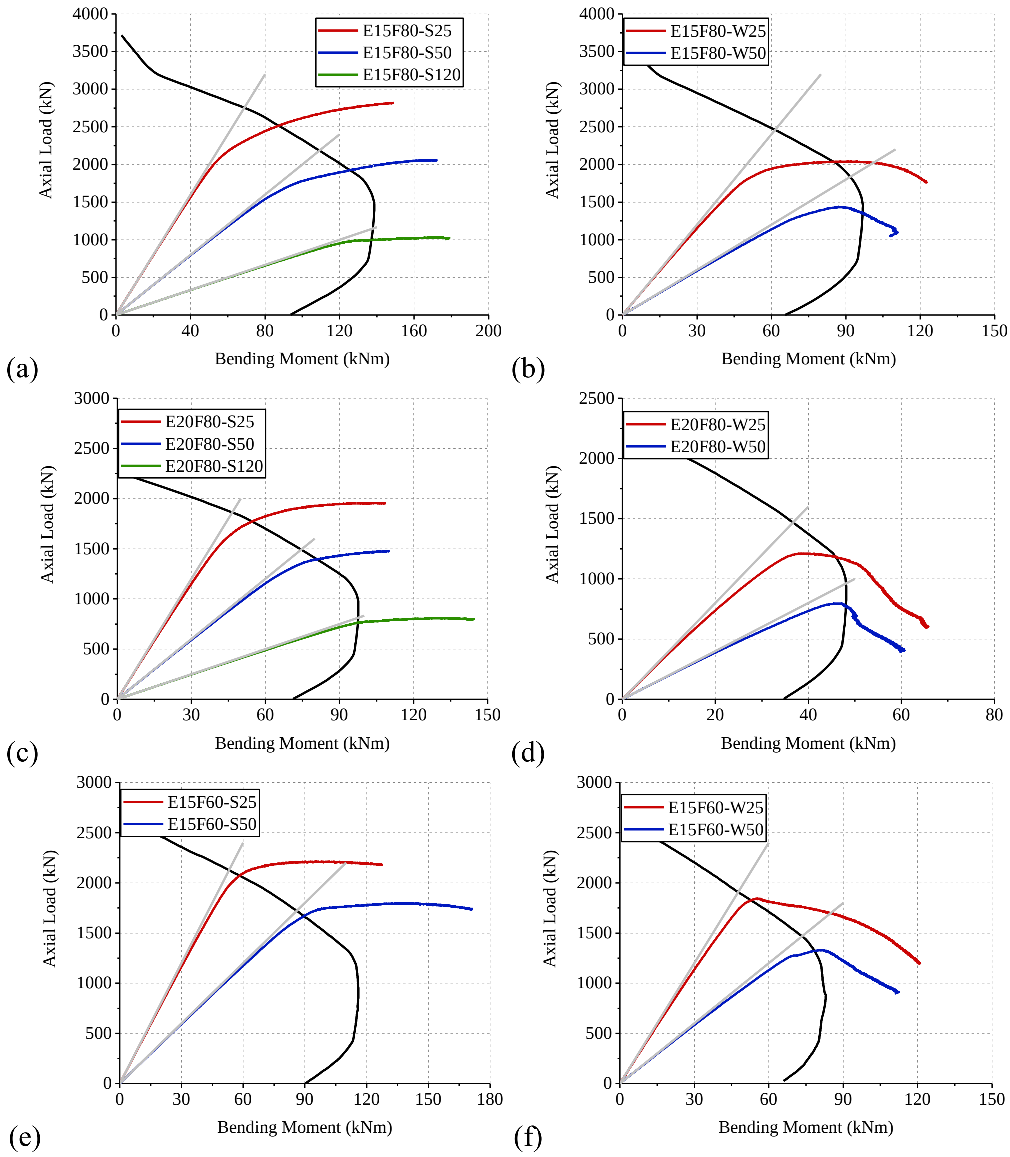

Figure 13 Experimental axial load-moment loading path vs. predicted *N*-*M* interaction diagram by section analysis

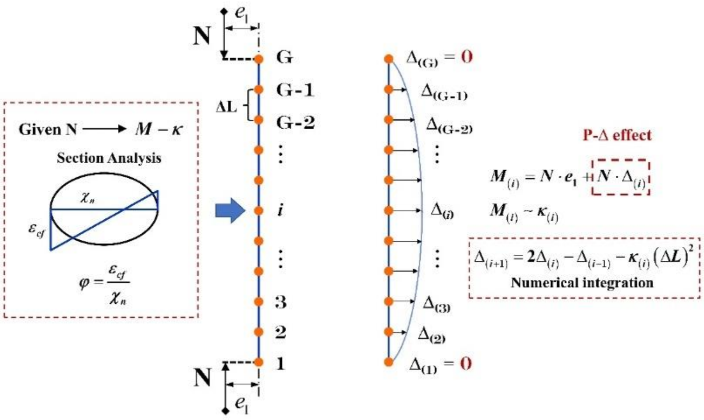

Figure 14 Illustration of the method of slender column analysis [plotted after Jiang and Teng (2012)]

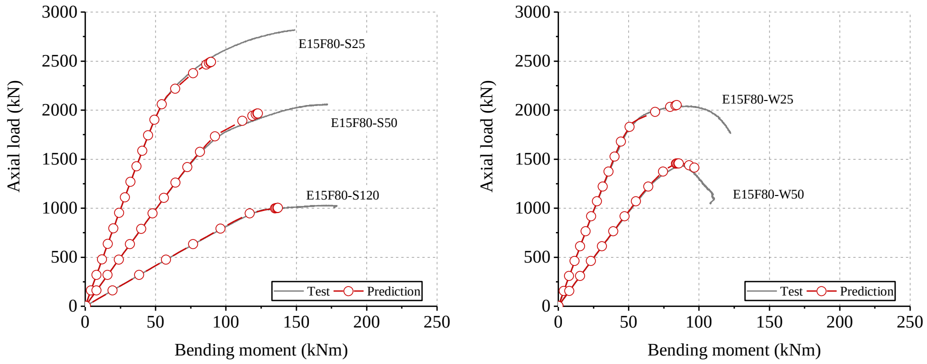

(a) Specimens of Group A

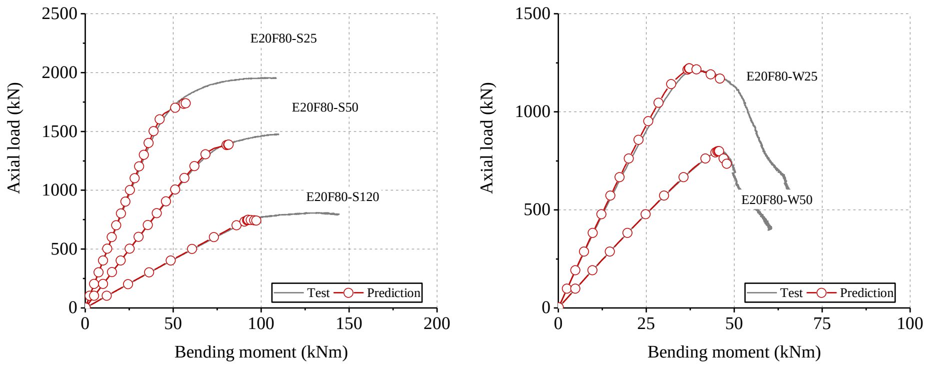

(b) Specimens of Group B

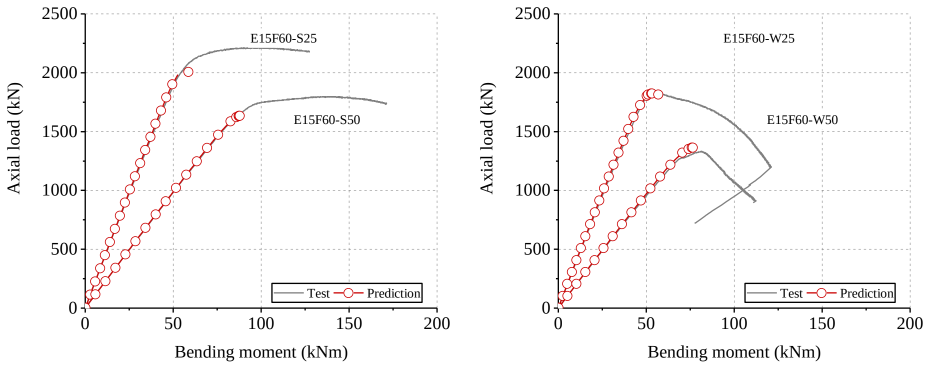

(c) Specimens of Group C

Figure 15 Predictions of column *N*-*M* paths with Model I stress-strain curves for concrete

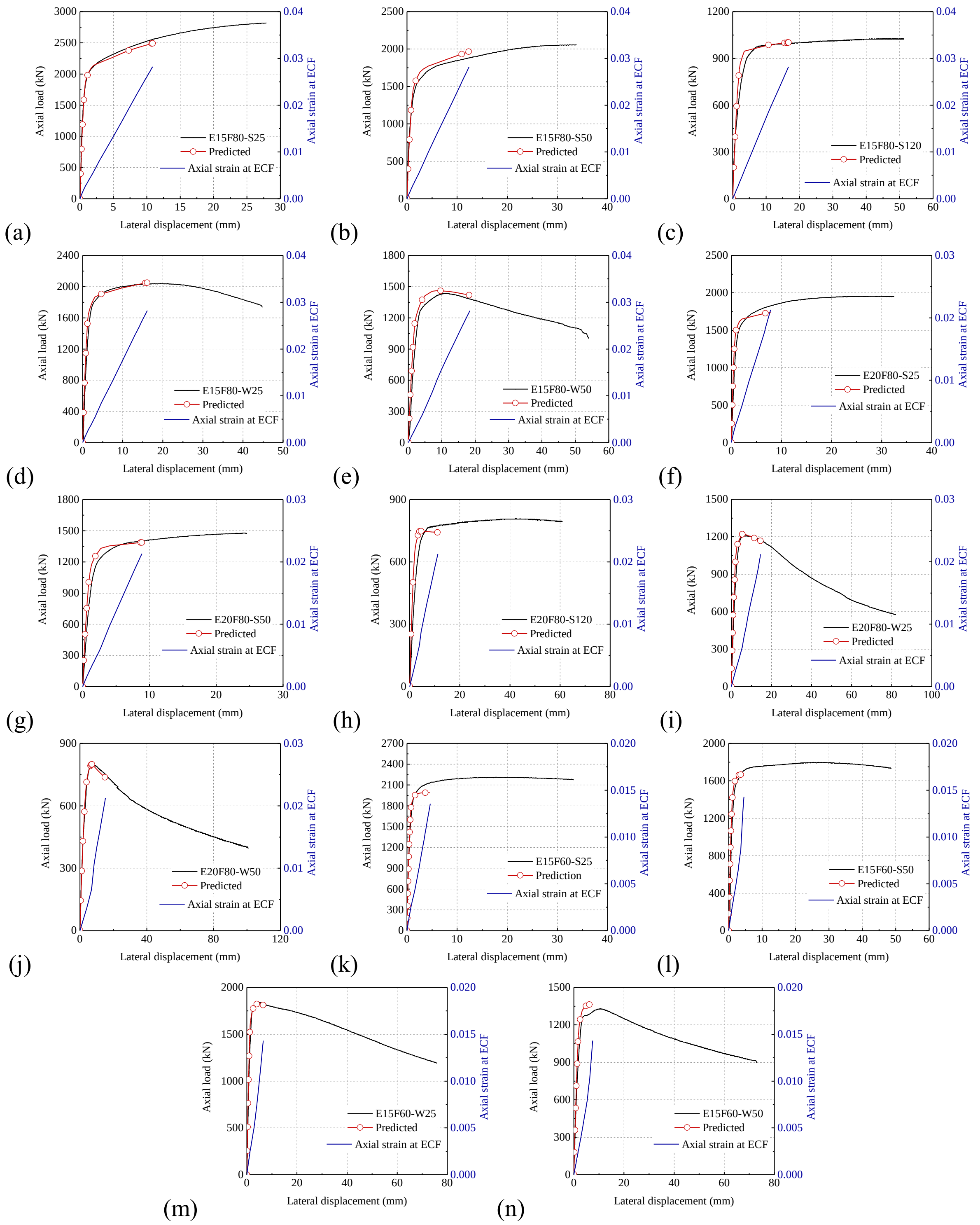

Figure 16 Predictions of axial load-lateral displacement curves with Model I stress-strain curves for concrete

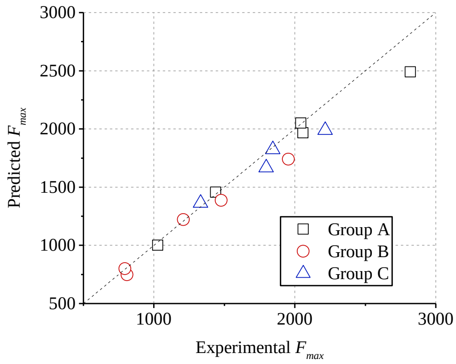

Figure 17 Comparison between experimental and predicted values for F_{max}

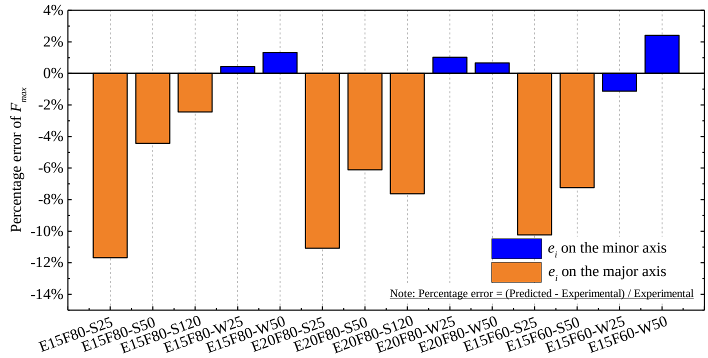

Figure 18 Percentage errors of predicted peak loads

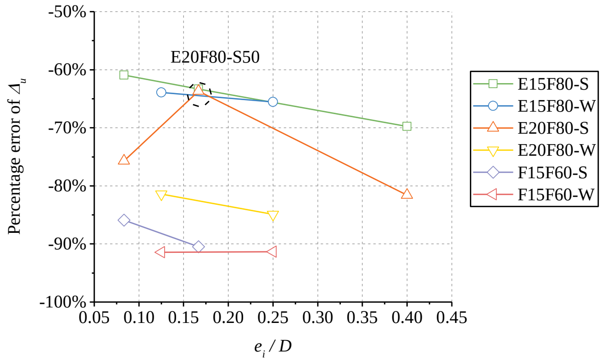

Figure 19 Percentage errors of predicted lateral displacements at ultimate state

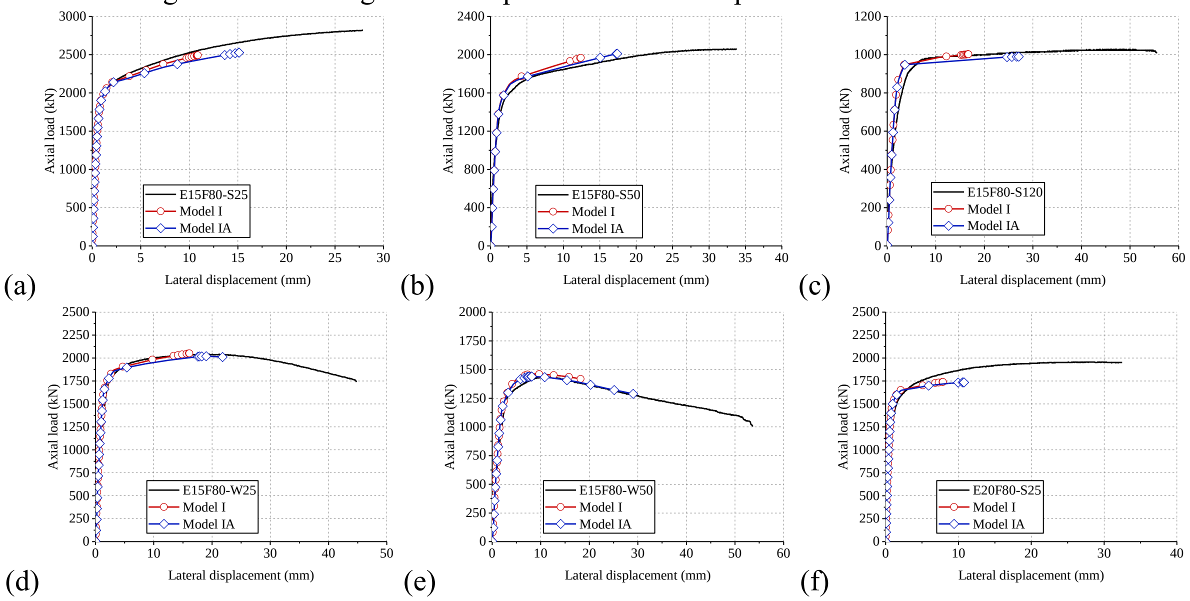

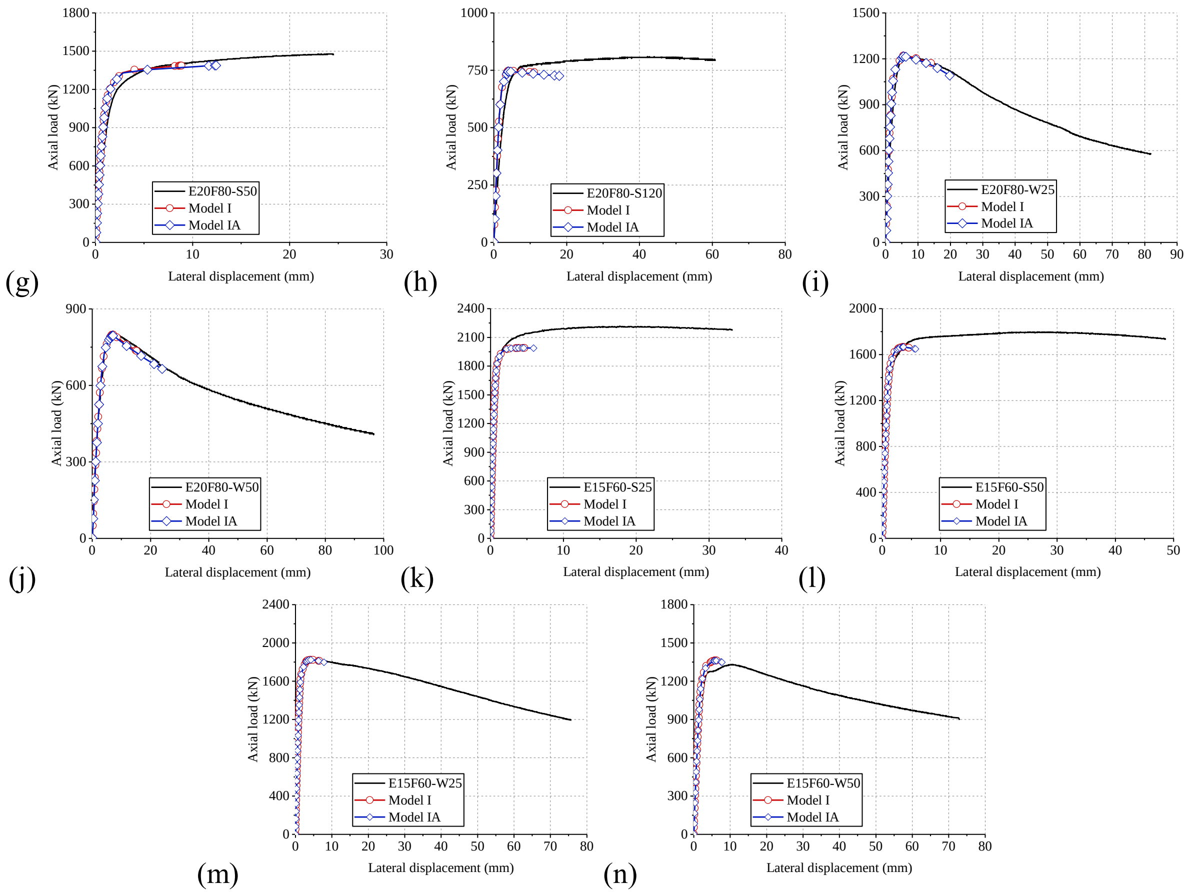

Figure 20 Predictions of axial load-lateral displacement curves with Model IA stress-strain curves for concrete

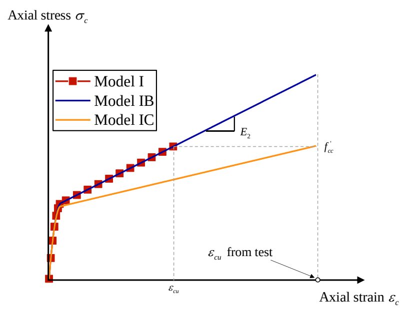

Figure 21 Two options for modifying the stress-strain model for confined concrete

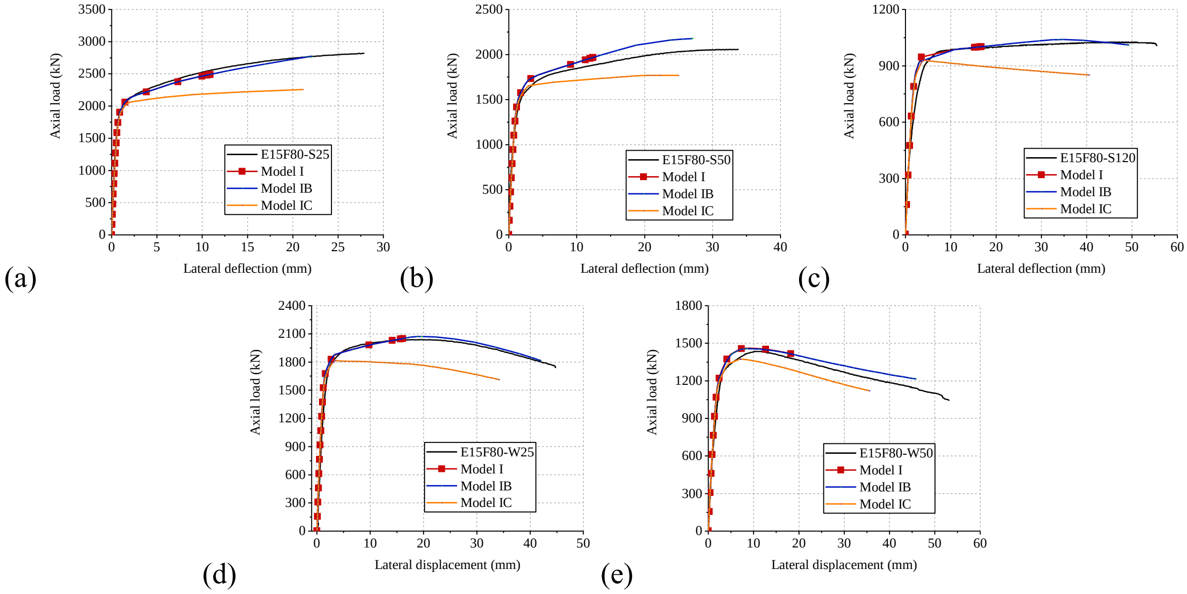

Figure 22 Predictions of axial load-lateral displacement curves for Group A specimens with the modified stress-strain models

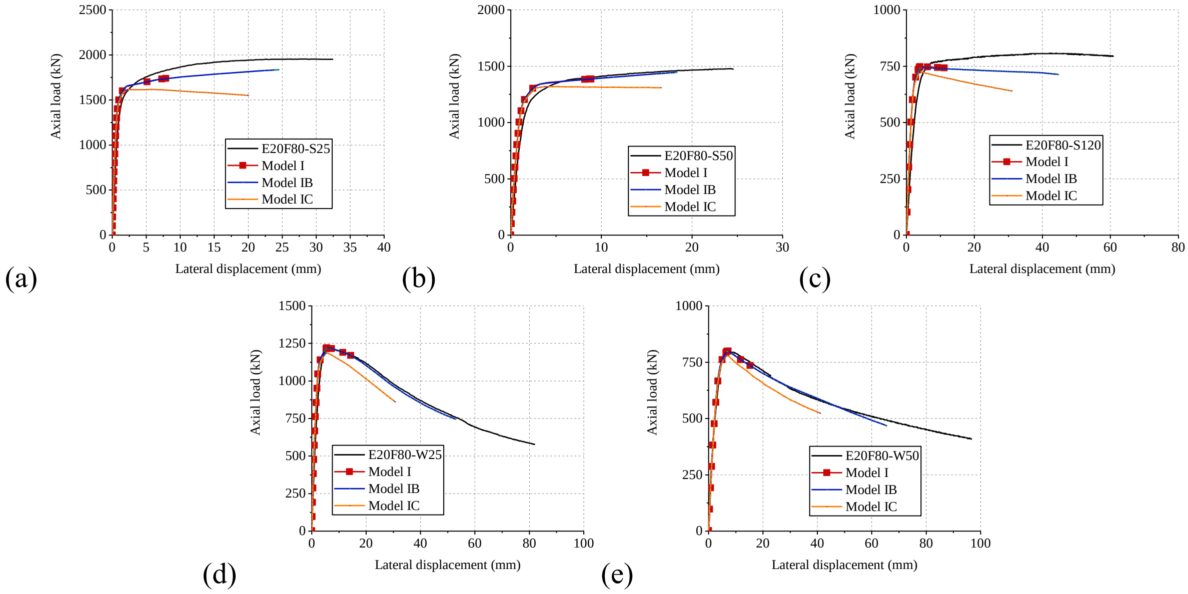

Figure 23 Predictions of axial load-lateral displacement curves for Group B specimens with the modified stress-strain models

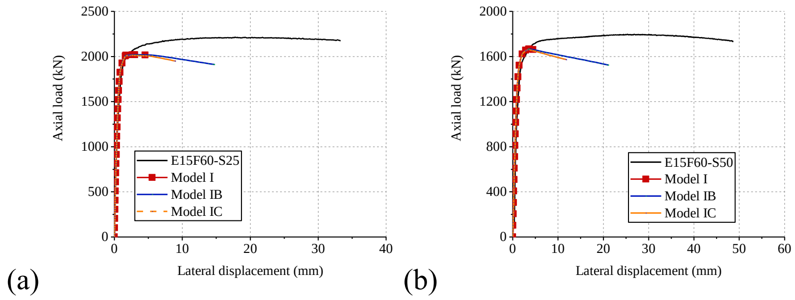

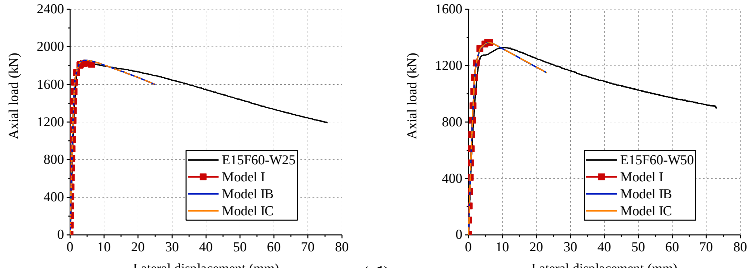

(c) (d)

Figure 24 Predictions of axial load-lateral displacement curves of Group C specimens with the modified stress-strain models

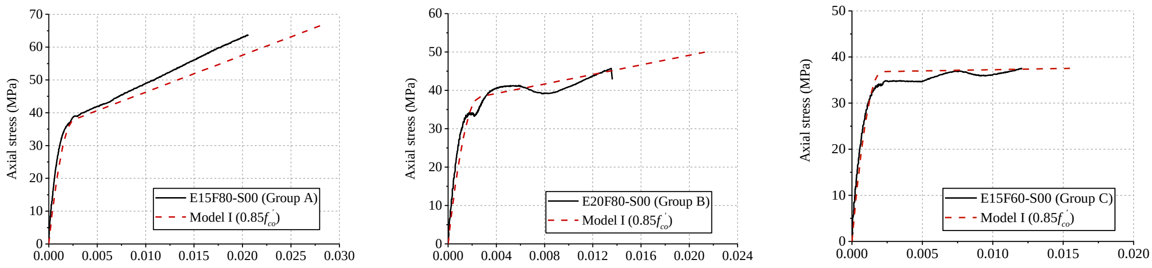

(a) (b) (c)

Figure A1 Comparison between experimental and predicted stress-strain curves of concrete in concentrically loaded column specimens

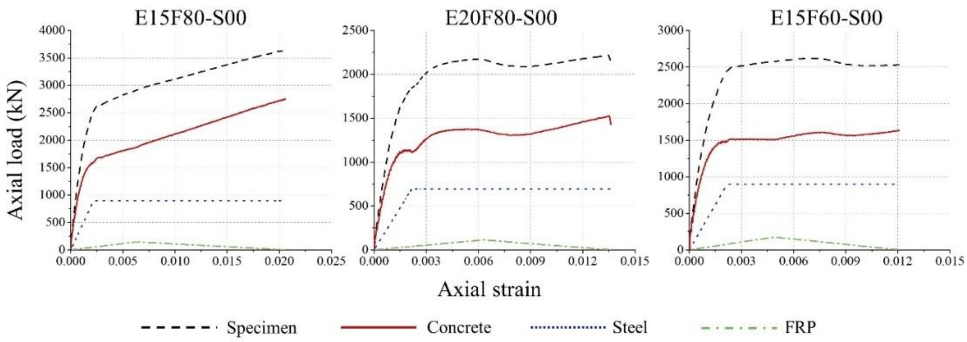

Figure A2 Axial load-axial strain curves of concentrically loaded columns: contribution by each component

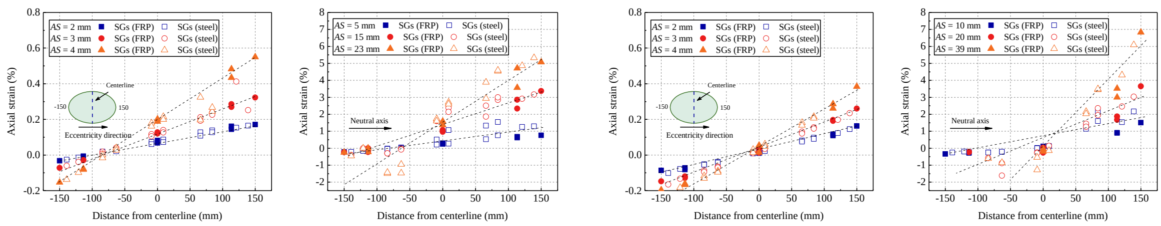

(a) E15F80-S50 (b) E15F80-S120

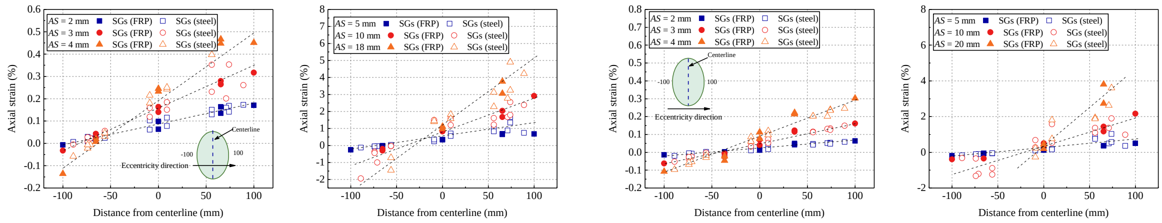

(c) E15F80-W25 (d) E15F80-W50

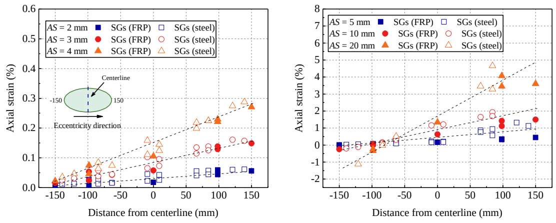

(e) E20F80-S25

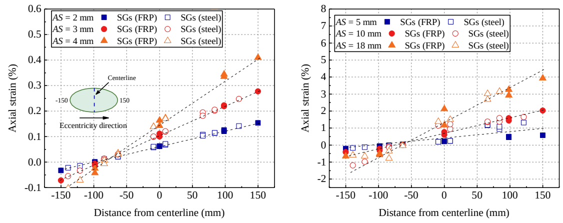

(f) E20F80-S50

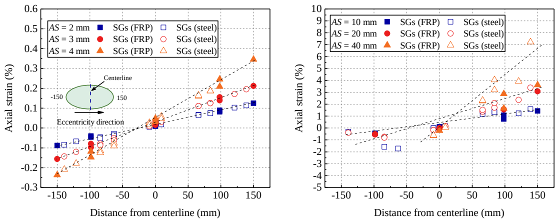

(g) E20F80-S120

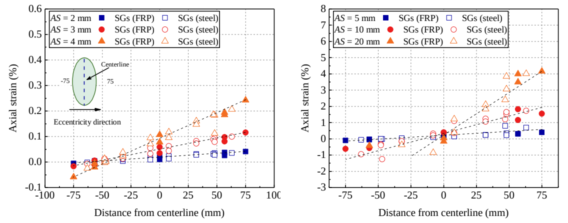

(h) E20F80-W25

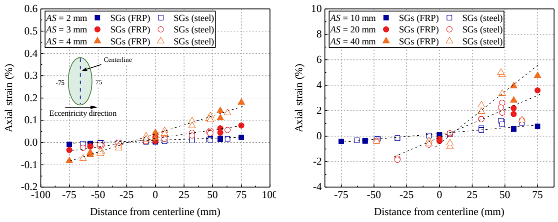

(i) E20F80-W50

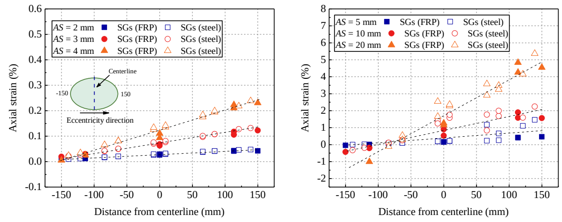

(j) E15F60-S25

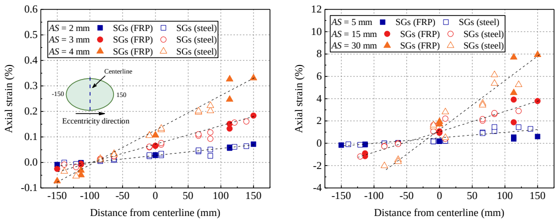

(k) E15F60-S50

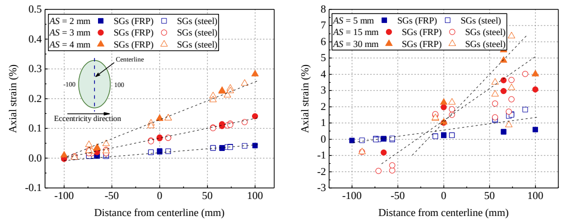

(l) E15F60-W25

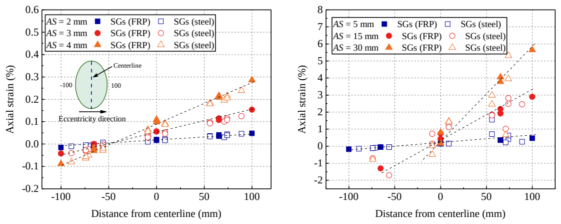

(m) E15F60-W50

Figure A3 Axial strain distributions in column specimens